

PAPER • OPEN ACCESS

Trends in mass utilization of a magnetically shielded Hall thruster operating on xenon and krypton

To cite this article: Leanne L Su *et al* 2024 *Plasma Sources Sci. Technol.* **33** 065008

View the [article online](#) for updates and enhancements.

You may also like

- [Development and validation of an iodine plasma model for gridded ion thrusters](#)
T Lafleur, L Habl, E Zorzoli Rossi *et al.*

- [The far-field plasma characteristics of LHT40 low-power Hall thruster for commercial aerospace applications](#)
Xinwei CHEN, , Zuo GU *et al.*

- [Argon admixture-driven enhanced ionization and performance of a 5 kW Hall thruster on krypton](#)
Dongho Lee, William P Brabston, Dan Lev *et al.*

HIDEN ANALYTICAL

Analysis Solutions for your **Plasma Research**

For Surface Science

- ▶ Surface Analysis
- ▶ SIMS
- ▶ 3D depth Profiling
- ▶ Nanometre depth resolution

The image shows three pieces of Hiden Analytical SIMS equipment. From left to right: a compact benchtop unit labeled 'Compact SIMS'; a larger workstation setup with a control console and a sample stage labeled 'SIMS Workstation'; and a more complex system with multiple components and a control console labeled 'Auto SIMS'.

■ Compact SIMS

■ SIMS Workstation

■ Auto SIMS

For Plasma Diagnostics

- ▶ Plasma characterisation
- ▶ Customised systems to suit plasma Configuration
- ▶ Mass and energy analysis of plasma ions
- ▶ Characterisation of neutrals and radicals

The image shows two plasma diagnostic tools. On the left is the 'ESPion' probe, which has a cylindrical body with a probe tip and is connected by a cable. On the right is the 'EQP Series' system, which consists of a large vertical control cabinet, a pump unit, and a probe assembly mounted on a mobile cart.

■ ESPion

■ HPR-60 MBMS

The image shows the 'HPR-60 MBMS' system, which is a large, modular plasma diagnostic setup. It includes a central control console, various vacuum components, and a probe assembly mounted on a mobile cart.

■ EQP Series

[Click to view our product catalogue](#)

■ Knowledge
■ Experience ■ Expertise

Contact Hiden Analytical for further details:

W www.HidenAnalytical.com
E info@hiden.co.uk

This content was downloaded from IP address 35.7.11.62 on 09/07/2024 at 18:02

Trends in mass utilization of a magnetically shielded Hall thruster operating on xenon and krypton

Leanne L Su*^{ID}, Thomas A Marks^{ID} and Benjamin A Jorns^{ID}

Department of Aerospace Engineering, University of Michigan, Ann Arbor, MI 48109, United States of America

E-mail: leannesu@umich.edu

Received 17 October 2023, revised 12 May 2024

Accepted for publication 31 May 2024

Published 17 June 2024



Abstract

The trends in mass utilization with increasing discharge voltage and current are investigated for a magnetically shielded Hall thruster operating on xenon and krypton. A 9 kW class shielded thruster is operated with discharge voltages from 300 to 600 V and discharge currents from 15 to 30 A on xenon and krypton. Experimental measurements of discharge current, thrust, anode efficiency, and ion velocity as a function of axial position are used to calibrate a multi-fluid 2D Hall thruster code at all operating conditions. The results of these calibrated simulations are employed to interrogate the plasma properties inside the thruster channel. A simplified 0D model for mass utilization evaluated on spatial averages of the simulated plasma parameters is employed to interpret the response of this efficiency mode with power for each propellant. It is found that with both higher voltage and current, mass utilization increases for both gases and their relative gap in this efficiency decreases. This can be attributed to the higher plasma densities and ionization rate coefficients at high voltage, and solely to higher plasma densities at high current. The driving factors for the increase in mass utilization are examined in the context of its nonlinear response to internal plasma properties. The behavior of mass utilization is also discussed in context of the gap in overall efficiency between the propellants. Finally, the implications of these results for improving the performance of high power Hall thrusters operating on krypton are examined.

Keywords: electric propulsion, Hall thruster, plasma propulsion, plasma physics, alternative propellants

1. Introduction

Hall thrusters are a type of electric propulsion (EP) device with high thrust density ($\sim 10 \text{ N m}^{-2}$), moderate specific impulse ($\sim 2000 \text{ s}$), and decades of in-space flight heritage. These

devices have been widely employed for near-Earth applications such as orbit-raising and station-keeping, and more recently, have also been baselined for deep space missions [1–3]. The advent of magnetic shielding, a technique that greatly extends the lifetimes of these devices [4, 5], has helped to expand their potential operating envelope and mission architectures.

As the use of Hall thrusters continues to increase, the selection of operating gas becomes a more pressing concern. The standard propellant of choice for these devices is xenon due to its high mass, low ionization energy, and chemical inertness. However, xenon is comparatively expensive, and there are relatively few providers internationally [6]. For this reason, there

* Author to whom any correspondence should be addressed.



Original Content from this work may be used under the terms of the [Creative Commons Attribution 4.0 licence](#). Any further distribution of this work must maintain attribution to the author(s) and the title of the work, journal citation and DOI.

has been substantial work in exploring alternative propellants for Hall thrusters such as krypton. Indeed, there are some EP companies that have extensively used this propellant on their thrusters [7], largely due to its lower price. However, there are two major limitations with krypton as a propellant choice: its poor storage density (0.53 mg cm^{-3} compared to xenon's 1.6 mg cm^{-3} [8]) and its historically lower performance [9–17]. The reduced storage density translates to larger tank requirements, while the poor performance of these devices may translate to more propellant and/or power required for a given mission.

Several studies have attempted to close the efficiency gap between xenon and krypton, most of which have been conducted on more conventional unshielded thrusters. The primary motivation behind these works has been the hypothesis that the performance gap is driven by krypton's lower mass utilization. Mass utilization is defined as a thruster's ability to convert incoming neutrals into ions that may then be accelerated to generate thrust. It has been suggested that Hall thrusters operating on krypton have lower mass utilization due to the smaller ionization cross-section of this gas. In an effort to improve krypton's mass utilization, previous works have changed Hall thruster geometry [15, 17] and operating conditions [11–18]. In particular, increasing the discharge voltage [14, 15, 18] and the discharge current [13, 14, 16] appears to help bridge the efficiency gap between these propellants on unshielded thrusters.

With that said, there are differences in the implementation of unshielded and shielded thrusters that may lead to different responses to changes in operating condition. There are notable variations in the internal plasma properties of these devices, such as how shielded Hall thrusters have higher electron temperatures and a downstream shift of the region in which ions are accelerated [5, 19, 20]. These differences may in turn impact our ability to close the efficiency gap with the same approaches applied to unshielded thrusters. In reference [9], for example, we showed that increasing the discharge voltage in a magnetically shielded thruster did not close the performance gap. This is in contrast to the behavior exhibited by unshielded thrusters in previous studies, where the efficiency gap does decrease at high voltage [14, 15, 18]. We proposed in this previous work that this discrepancy may be due to the differences in electron temperature between the magnetic field topologies, but were unable to directly validate this theory absent internal measurements of the thruster.

More recently, we have investigated increasing the discharge current on shielded Hall thrusters [21, 22] and saw the performance gap close at sufficiently high currents. This behavior is in line with observations on unshielded thrusters [13, 14, 16]. In keeping with these other studies, we attributed the improvement of performance in this work to the presence of more charge carriers at high currents, facilitating more ionization and therefore better mass utilization. With that said, as in the case of our voltage study, we lacked direct plasma measurements needed to confirm this hypothesis. Ultimately,

while we have physical arguments for the behavior of the performance gap between propellants on shielded thrusters, there is key missing data for validating these arguments. There is an apparent need to directly investigate the plasma properties within the thruster as a function of operating condition and propellant.

The goal of this work is to generate these types of internal measurements and relate them to our understanding of the thruster performance trends. To this end, we adopt an approach using multi-fluid simulations that are calibrated against limited experimental data to infer internal plasma properties [23]. Our decision to use this method stems from the fact that internal probes are perturbative and may obscure physical trends [24].

This paper is organized as follows. In section 2, we overview the operation of a Hall thruster and outline a 0D model for how the mass utilization responds to changes in internal plasma properties. Next, in section 3, we describe the experimental setup, including the thruster and facility, the numerical code employed, and the diagnostics used to obtain thruster measurements. Then, in section 4, we present the results of our experimental measurements and calibrated simulations. We also evaluate our 0D model for mass utilization and compare it to experimental trends. In section 5, we discuss our findings by using the simulation outputs to interrogate the physical origins of the difference in performance between krypton and xenon. Finally, in section 6, we conclude by summarizing our work.

2. Theory

In this section, we describe the physics of Hall thruster operation and a 0D law for mass utilization that scales with internal plasma properties. Figure 1 shows an illustration of typical Hall thruster operation. These annular crossed-field plasma devices apply a voltage, V_d , between the conductive anode and hollow cathode, generating a discharge current, I_d , within the channel, and an electric field, \vec{E} , that points axially downstream. The cathode emits electrons which follow the electric field through the discharge channel toward the anode, while a neutral propellant is injected at the anode. A radial magnetic field, \vec{B} , confines the electrons in an azimuthal drift, which ionizes the injected neutrals. The resulting ions then follow the electric field downstream and produce thrust, the force by which the thruster is able to move. The cathode also injects sufficient electrons to preserve neutrality downstream.

A key metric for evaluating thruster performance is the anode efficiency, the ratio of thruster jet power to total electrical input power:

$$\eta_a = \frac{T^2}{2\dot{m}_a P_d}, \quad (1)$$

where \dot{m}_a is the neutral flow into the channel through the anode and $P_d = V_d I_d$ is the discharge power. This term can in turn be expressed as the product of a series of efficiency modes representing different loss mechanisms within the thruster [25–28]. As introduced in section 1, the main driver for the efficiency

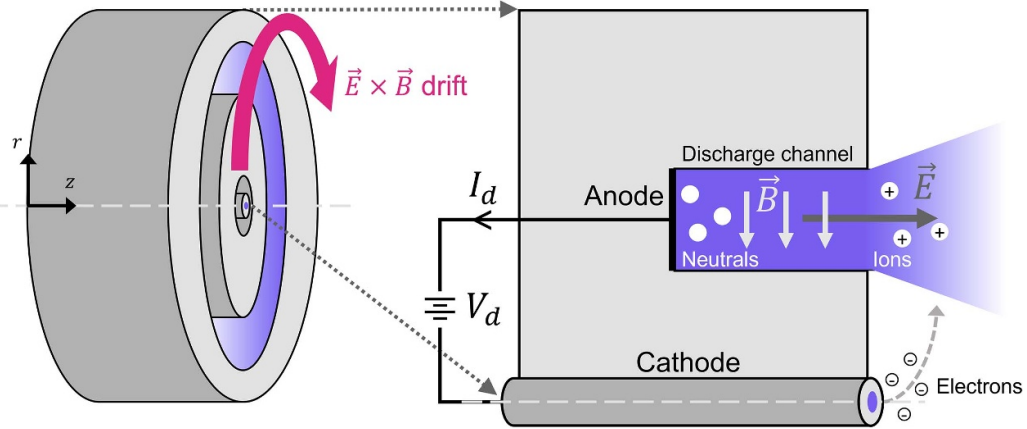


Figure 1. Operation of a typical Hall thruster.

gap between xenon and krypton that has been hypothesized to date is the mass utilization, defined as

$$\eta_m = \frac{\dot{m}_b}{\dot{m}_a}, \quad (2)$$

where \dot{m}_b is the ion beam mass flow rate and \dot{m}_a is the neutral flow rate into the channel. We note that this is the mass utilization of the anode, not the total device, as it does not account for cathode flow. Physically, this efficiency mode captures the ability of the thruster to ionize incoming neutrals. Given the purported role of mass utilization in driving the efficiency gap between xenon and krypton, we focus on this efficiency mode with the understanding that $\eta \propto \eta_m$.

A key goal of this work is to motivate physically how mass utilization depends on internal plasma properties, and in turn, how this may help explain the disparity between xenon and krypton performance on shielded thrusters. To this end, we rewrite the mass utilization efficiency as

$$\eta_m = 1 - \frac{\dot{m}_n(L)}{\dot{m}_n(0)} \approx 1 - \frac{n_n(L)}{n_n(0)}, \quad (3)$$

where \dot{m}_n is the neutral flow and n_n is the neutral density. Here, the values in parentheses denote axial locations z , where $z=0$ is the anode and $z=L$ represents the location where ionization has effectively ended. We have invoked in this derivation the definition of mass flow rate $\dot{m}_n = m_n n_n v_n A_{ch}$, where m_n is the mass of the neutral (approximately equivalent to the mass of the ion m_i), v_n is the axially-averaged neutral velocity, and A_{ch} is the channel area. We note here that the approximate equivalence in this expression is because we have assumed both of them experiencing slight variations from $z=0$ to $z=L$. This change is more drastic in the neutral velocity, which can vary by $\sim 50\%$ through the channel [29]; for simplicity in our analysis, we treat this value as constant and find it to have minimal impact on our results.

To formulate an expression for the neutral density at the end of the region of interest, we consider the quasi-1D continuity equation for neutrals in the thruster channel at steady-state:

$$v_n \frac{\partial n_n}{\partial z} = -k_{iz} n_e n_n, \quad (4)$$

where k_{iz} is the rate coefficient for ionization averaged over a Maxwellian electron energy distribution [30–32] and n_e is the electron or plasma density. All quantities in this expression except neutral density are averaged over the channel area. We next make the strong assumption that the plasma properties are approximately constant axially in the channel such that we can write

$$n_n(L) = n_n(0) \exp \left[-\frac{\langle k_{iz} \rangle \langle n_e \rangle}{\langle v_n \rangle} \alpha L \right], \quad (5)$$

where $\langle x \rangle$ denotes a value averaged over the axial range from $z=0$ to $z=L$. Here we have introduced a scaling factor $\alpha < 1$ to account for the fact that the ionization region length is shorter than the channel length.

Physically, equation (5) suggests that the neutral density should decay exponentially with distance from the anode. This stems from the fact that the neutral population is depleted by ionization. While the assumptions made in deriving this expression are admittedly strong, the exponential decay of neutral density has been previously observed in Hall thrusters simulations [33, 34]. This lends credibility to our simplifications. Moreover, the simplified scaling of neutral density and its dependence on spatially-averaged properties lends itself to an intuitive physical interpretation.

To this end, we can substitute equation (5) into equation (3) to yield

$$\eta_m = 1 - \exp \left[-\frac{\alpha L}{\lambda_{iz}} \right], \quad (6)$$

where we have defined an ionization mean free path (assuming only singly-charged ions are produced) as

$$\lambda_{iz} = \frac{\langle v_n \rangle}{\langle k_{iz} \rangle \langle n_e \rangle}. \quad (7)$$

Equations (6) and (7) provide a framework for understanding the differences between the scaling of xenon's and krypton's mass utilization as well as the various potential techniques for

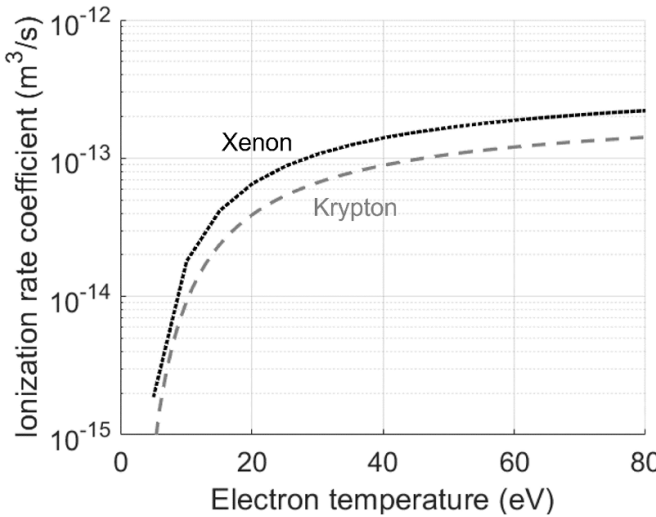


Figure 2. Ionization rate coefficient as a function of electron temperature for xenon and krypton [30–32].

improvement. For example, we can use this equation to analyze the ratio of mean free paths of xenon and krypton. First, we note that the neutral velocity scales as $v_n \propto 1/\sqrt{m_i}$ assuming that the neutral temperature is the same between gases and approximating the neutral and ion masses as equal. Second, assuming that the current remains constant between propellants, conventional scaling laws would suggest that the plasma density in the near-field scales with mass, $n_e \propto \sqrt{m_i}$ [22]. The ratio between ionization mean free paths then becomes

$$\frac{\lambda_{iz}(\text{Xe})}{\lambda_{iz}(\text{Kr})} = \frac{\langle k_{iz}(\text{Kr}) \rangle}{\langle k_{iz}(\text{Xe}) \rangle} \frac{m_i(\text{Kr})}{m_i(\text{Xe})}. \quad (8)$$

The mass of xenon is 131.3 amu in comparison to krypton's 83.8 amu. In addition, as seen in figure 2, the ionization rate coefficient for xenon at a given electron temperature is higher than it is for krypton. This ionization rate coefficient, obtained by integrating the ionization cross section over a Maxwellian electron energy distribution function [30–32], has a nonlinear dependence on electron temperature. Given these ratios and the simplifying assumptions we have made, equation (8) shows that the ionization mean free path of krypton is longer than that of xenon. This translates to lower mass utilization and lower performance for krypton.

It is apparent from equation (8) that at a given operating condition, the mass utilization of krypton will always be worse than that of xenon due to its lower mass. However, because the mass utilization exponentially approaches unity with increasing channel length or decreasing ionization mean free path (equation (6)), adopting strategies to improve this parameter for both gases will eventually close the gap. In principle, this can be accomplished by varying the geometry or operating condition of the thruster. For example, lengthening the channel has been shown to improve ionization in thrusters operating on krypton [15, 17]. On the operational side, increasing the discharge voltage has been shown to raise the electron temperature [28], which consequently increases the ionization

rate coefficient. Alternatively, increasing the discharge current increases the plasma density, reducing the ionization mean free path (equation (7)). As discussed in section 1, these three techniques are all effective in closing the performance gap on unshielded thrusters.

However, to fully elucidate the physics driving the responses to operational changes in shielded thrusters, we need direct measurements of plasma parameters such as the plasma density, electron temperature/ionization rate coefficient, and neutral velocity. This need is underscored by equation (6), which we subsequently use as a framework for assessing the mass utilization of the thruster. We describe in the following section how we obtain the necessary measurements to evaluate it.

3. Methodology

In order to infer the internal properties of the channel, we use a high-fidelity simulation code calibrated against non-invasive experimental measurements. The premise is that if this model can be made to match key metrics of the thruster that are experimentally accessible, we can use it as a virtual diagnostic to determine other plasma properties of interest (equation (6)) that are difficult to measure with traditional probes without perturbing the plasma [23, 24, 35].

3.1. Thruster and facility

For this study, we employed the H9, a 9 kW class magnetically shielded Hall thruster designed in a collaboration among the University of Michigan (UM), Jet Propulsion Laboratory, and Air Force Research Laboratory [19, 36]. This thruster employs a boron nitride channel, a center-mounted LaB₆ cathode, graphite pole covers, and a stainless steel anode. The H9 has been experimentally characterized on both xenon and krypton as the subject of many performance and plasma property measurements [9, 10, 19, 36–38]. The nominal operating envelope of the H9 on xenon is approximately discharge powers of 4.5–12 kW, specific impulses of 1800–3000 s, thrusts of 290–700 mN, and total efficiencies of 55%–70%. The typical operating envelope on krypton is discharge powers of 4.5–9 kW, specific impulses of 1900–2700 s, thrusts of 260–350 mN, and total efficiencies of 45%–55%. We operated the thruster in the Alec D. Gallimore Large Vacuum Test Facility at UM, a 6 m diameter by 9 m long chamber [39]. Pressure measurements were taken with a Stabil ion gauge located 1 m away from the thruster in the exit plane following best practices [40]. We ran this thruster at the conditions shown in table 1 with a constant cathode flow fraction of 7% and the cathode electrically tied to thruster body [41]. The magnetic field in this table is scaled to the nominal field strength at the baseline condition of 300 V, 15 A for xenon.

We note that there are two sets of flow rates and pressures shown in table 1. The first column denotes settings during performance measurements from our previous work [9, 10, 38],

Table 1. Operating conditions and base pressures for the H9. The volumetric flow rates are calculated with STP conditions assuming a temperature of 25 °C.

Species	Voltage (V)	Current (A)	Power (kW)	B-field ratio (%)	Thrust test mass flow (mg s ⁻¹ , sccm)	Thrust test pressure (μtorr)	Ion vel. test mass flow (mg s ⁻¹ , sccm)	Ion vel. test pressure (μtorr)
Xe	300	15	4.5	100	14.8, 165	4.8	14.7, 164	5.4
Xe	400	15	6	100	15.4, 172	5.8	15.5, 172	5.8
Xe	600	15	9	100	16.3, 181	6.2	16.3, 181	6.4
Xe	300	20	6	100	18.5, 206	5.8	18.5, 206	6.6
Xe	300	30	9	100	—	—	25.3, 281	8.8
Kr	300	15	4.5	100	11.8, 207	4.6	11.2, 195	5.4
Kr	400	15	6	112.5	11.5, 201	4.5	11.2, 196	5.6
Kr	600	15	9	112.5	12.5, 218	4.9	12.4, 217	6.4
Kr	300	20	6	87.5	15.3, 268	5.8	14.5, 253	6.8
Kr	300	30	9	87.5	—	—	20.9, 366	7.8

while the second column denotes settings during a campaign to measure ion velocities (section 3.3.2). We attribute the slight differences in these values to minor changes in test setup, including differences in the active number of cryopumps used (14–16 during performance measurements, 17 during ion velocity measurements) and how long the thruster had been operating before measurements were taken. With that said, the flow rates are within 6% and the pressures are within 30% of each other, which is within normal experimental variation.

3.2. Hall thruster model

We used Hall2De, a 2D axisymmetric multi-fluid/particle-in-cell (PIC) Hall thruster code developed at the Jet Propulsion Laboratory [23, 35, 42], as our virtual diagnostic to infer internal plasma properties.

3.2.1. Model physics. We briefly describe the code here with additional information in [23]. The code has different solvers for each species. Hall2De treats the electrons as a fluid, employing a generalized Ohm's law formulation for the momentum balance and an equation for the time evolution of the internal electron energy. These electron equations of motion are solved on a mesh aligned with the applied magnetic field. This magnetic-field-aligned mesh (MFAM) helps reduce numerical diffusion resulting from the anisotropy of electron dynamics in a magnetized plasma.

Hall2De has the capability to model the ions either kinetically using the PIC method or as a series of fluids. In this present work, we used the fluid version of the code, which solves fluid mass, momentum, and energy equations for several ion species, differentiated by the charge state and origin. We include three ion charge states (singly-, doubly-, and triply-charged) for each of two ion fluids, yielding a total of six ion populations. The first ion fluid tracks ions born in the main thruster beam, while the second is comprised of ions emitted from the cathode or born in the cathode plume. As ions in a Hall thruster are unmagnetized by design, their equations of motion are solved on a more standard rectilinear/Cartesian

grid. For the neutrals, the code uses a collisionless line-of-sight view-factor algorithm on the same mesh as the ions.

3.2.2. Anomalous electron transport. As with all fluid- or hybrid-based approaches to thruster modeling [43], Hall2De underpredicts the cross-field electron current when considering only classical collisional effects on electron dynamics. This is accounted for by introducing an effective or ‘anomalous’ electron collision frequency into the generalized Ohm's law: $\nu_e = \nu_{e,\text{class}} + \nu_{e,\text{anom}}$, where ν_e is the total electron collision frequency, $\nu_{e,\text{class}}$ is the electron collision frequency due to classical electron collisions, and $\nu_{e,\text{anom}}$ is the anomalous collision frequency. By adjusting this collision frequency, it is possible to increase the effective electron transport across the magnetic field and therefore bring the electron current more in line with what is measured experimentally. In this work, we employ a static model in which the anomalous collision frequency is prescribed as a piecewise function of axial distance from the anode along channel centerline:

$$\log \frac{\nu_{e,\text{anom}}}{\omega_{ce}} = \begin{cases} c_1 & z \leq z_1 \\ c_i + (c_{i+1} - c_i) \frac{z - z_i}{z_{i+1} - z_i} & z_i < z \leq z_{i+1} \\ c_4 & z > z_4 \end{cases} \quad (9)$$

In the above, i is an index that ranges from 1 to 4, z is axial distance from the anode, (z_i, c_i) are adjustable free parameters, and ω_{ce} is the electron cyclotron frequency. In figure 3, we show a notional example of such a collision frequency profile defined by equation (9). We assume that the inverse anomalous Hall parameter, $\nu_{e,\text{anom}}/\omega_{ce} = \Omega_e^{-1}$, varies only with the axial location z and is constant in the radial direction. In practice, the user can adjust the eight free parameters in this model to match the experimentally measured quantities of interest such as current and thrust. Similar piecewise anomalous transport profiles have been previously used to simulate a number of Hall thrusters in Hall2De [35, 44].

Because the form for the anomalous collision frequency is not known *a priori*, Hall2De and other Hall thruster codes are not fully predictive. However, once a collision frequency

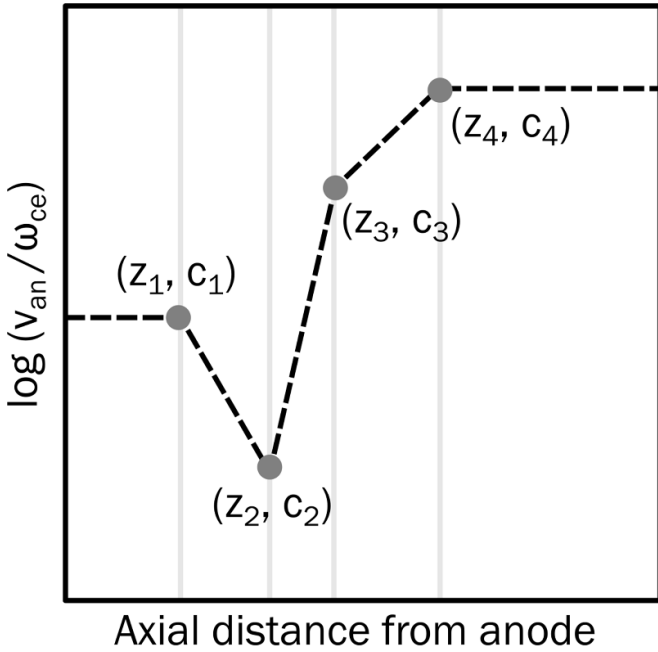


Figure 3. Notional anomalous collision frequency profile according to equation (9).

profile is prescribed, the physics in the model as represented by the governing equations for the electrons, ions, and neutrals are closed. Our overarching assumption is that if the collision frequency can be calibrated by matching measurable quantities of interest, the other plasma properties produced by the code will also represent those of the actual thruster. In this sense, the model can be used as a virtual diagnostic for plasma parameters within the thruster and is thus an invaluable tool for accessing difficult-to-measure quantities. We note here that a weakness of this approach is the relatively poorly-calibrated electron temperature in the simulations, which is determined by the electron energy equation. Previous simulation efforts have revealed the difficulty of calibrating both electron temperature and ion velocity simultaneously [35, 42]. Given the availability of the ion velocity profiles, we use this as our calibration metric.

3.2.3. Metrics for calibrating anomalous collision frequency. As discussed in the preceding section, it is necessary to have experimental measurements to match to simulation outputs. For this effort, we use the discharge current, thrust, anode efficiency, and ion velocity profile. The current and thrust are direct outputs of the code. However, matching experimental thrust values to simulation requires tuning of parameters (such as anomalous transport in the cathode plume) that were beyond the scope of this investigation. In order to focus on the key factors that explain the difference between xenon and krypton performance, these parameters were not exhaustively studied, and instead a constant empirical thrust correction factor of 1.09 was used to adjust the thrust for all simulations.

Hall2De is also capable of predicting ion velocity as a function of axial distance from the anode. This is a property that we are able to measure experimentally with non-invasive

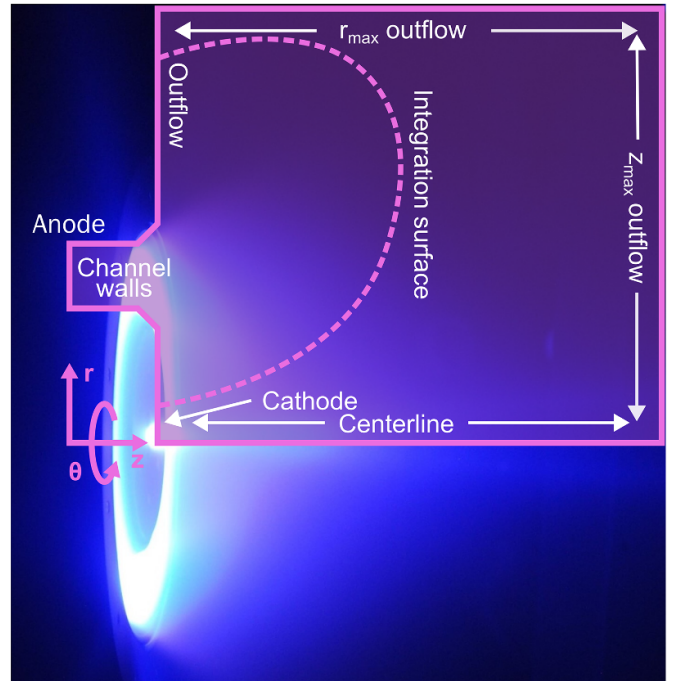


Figure 4. Hall2De simulation domain overlaid atop H9 operating on krypton at 300 V, 15 A.

techniques as described in section 3.3.2. This set of spatially-resolved data has become one of the standard references for calibrating the electron collision frequency as it varies axially [35]. To quantify the agreement between the simulation and the experimentally-measured ion velocities, we define the integrated velocity residual (IVR) [44]:

$$\text{IVR} = \sqrt{\frac{\int_{z_0}^{z_N} (u_{i,\text{exp}}(z) - u_{i,\text{sim}}(z))^2 dz}{\int_{z_0}^{z_N} u_{i,\text{exp}}^2(z) dz}}, \quad (10)$$

where z_0 is the location of the first experimental measurement and z_N is the last. We note here that we neglect uncertainty in the experimental data when calculating IVR.

When we calibrate the collision frequencies in the code, we manually adjust the coefficients in equation (9) and systematically compare the code outputs to these four metrics. The requirements we adopt for a ‘calibrated’ simulation are

- (i) Discharge current, I_d , within 1%,
- (ii) Thrust, T , within uncertainty of experimental data,
- (iii) Anode efficiency, η_a , within uncertainty of experimental data,
- (iv) IVR below 0.12.

3.2.4. Simulation domain. In figure 4, we show the simulation domain for Hall2De superimposed on an image of the H9 thruster, including the boundaries and coordinate system. The total simulation domain for the thruster extended approximately eight channel lengths downstream of the anode and eight channel lengths radially outward from the center of the thruster.

Table 2. Numerical parameters employed in this work.

Parameter	Value
Number of cells (MFAM)	1949
Number of cells (rectilinear grid)	1684
Maximum charge state	3+
Number of fluids	2
Cathode flow fraction	7%
Cathode ionization fraction	5%
Cathode electron temperature	3 eV
Wall temperature	500 °C
Timestep	20–50 ns
Max simulated time	3 ms

We summarize in table 2 simulation parameters for Hall2De used in this investigation. We used a field-aligned mesh with 1949 cells and a rectilinear grid with 1684 cells. This grid resolution was selected to balance numerical accuracy with speed, owing to the need to run large numbers of simulations sequentially in order to calibrate the anomalous collision frequency profiles. As with experimental testing, the cathode flow fraction was set to 7%. The ionization fraction and electron temperature at the cathode orifice were set to 5% and 3 eV, respectively. These values are in line with experimental measurements of the cathode employed in the H9 [45]. We assumed the neutrals were emitted with an average speed given by a half-Maxwellian distribution in one direction at 400 K, $v_n = \sqrt{2k_B T / \pi m_i}$, resulting in a velocity of 129.1 m s⁻¹ for xenon and 161.6 m s⁻¹ for krypton. The channel wall temperatures were set to 773 K (500 °C). While the channel temperature likely has some dependence on the operating power, we have kept it constant in our analysis and found that thrust and ion velocity were relatively insensitive to changes in inlet velocity. We also note here that we used the Sagdeev model for anomalous transport in the cathode plume [46], which is another tunable parameter that may be a fruitful subject of future investigation.

We ran each simulation for 3 ms of simulated time with a timestep between 20 and 50 ns. This total runtime was sufficient for the ion velocity, discharge current, and thrust to converge in a time-averaged sense. We then evaluated time-averaged properties using the last millisecond of simulation time. Three milliseconds of simulation time corresponded to between 5 and 20 hours of wall time per simulation using 8 CPU cores. While Hall2De is designed to run on ordinary desktop computers, we conducted the majority of the simulations using the Great Lakes supercomputing cluster at the University of Michigan. This enabled us to run many simulations in parallel, reducing the amount of user time required to calibrate each condition.

3.3. Generating data for model calibration

In this section, we describe the experimental methods we used to obtain performance measurements and ion velocity profiles to calibrate to in Hall2De.

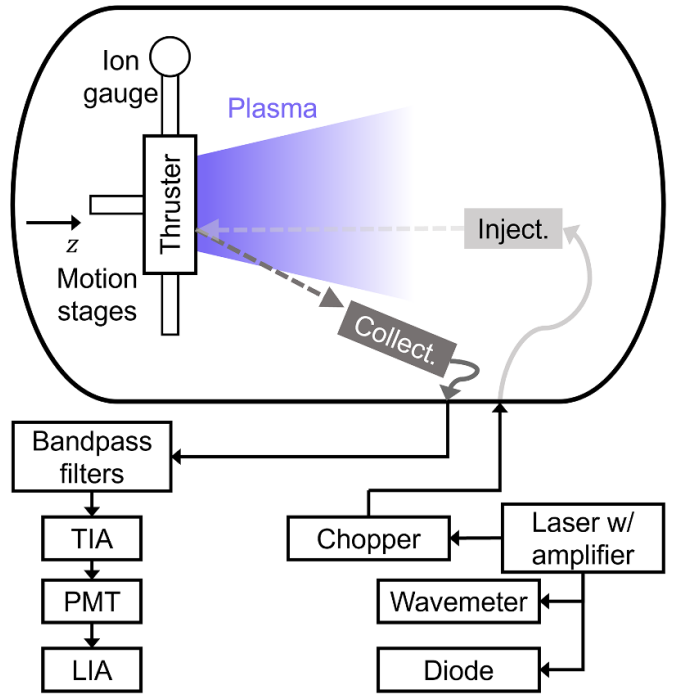


Figure 5. Notional diagram of LIF setup. Note that in this diagram, light moves from right to left.

3.3.1. Performance. The thrust and efficiency data we used for calibration originates from our previous study [9, 10]. In this work, we used a null-type inverted pendulum thrust stand to measure the thrust of the H9. We were then able to infer anode efficiency from these measurements. We note here that we used the flow rates and pressures (table 1) from this previous campaign as inputs to Hall2De. This decision was made based on the assumption that minor changes in flow rate and pressure would impact performance predictions more than they would the ion velocity profile.

3.3.2. Ion velocity profiles. We used laser-induced fluorescence (LIF), a non-invasive diagnostic, to measure the ion velocities along centerline in the H9. We used an excitation wavelength to target the transition of a metastable state and measure the intensity of the resultant fluorescence. By varying the injection wavelength, we were able to produce a Doppler-broadened lineshape of this transition resulting in a distribution of ion velocities [47–51]. The relationship between velocity and wavelength is $v = c(1 - \lambda / \lambda_0)$, where v is velocity, c is the speed of light, λ is the injection wavelength, and λ_0 is the central wavelength of the transition.

We used the 728.98 nm in air transition for Kr II that fluoresces at 473.90 nm [52]. For the Xe II setup, we used the 834.72 nm in air transition that fluoresces at 541.91 nm [52]. These transitions have been previously employed for Hall thruster testing [48–51, 53, 54]. Figure 5 shows the setup, including optical path, of our LIF injection scheme for both gases. The system started with a laser head that differed based on injection wavelength. For the krypton transition, we used

a TOPTICA TAprio tunable diode laser and tapered amplifier system with a center wavelength of 729.18 nm, maximum output power of 500 mW, and a mode hop free tuning range of 56 GHz. For the xenon transition, we used a Newport TLB-6700 diode laser and a TA-7600-LN tapered amplifier. A wavemeter precisely measured the wavelength of a probe beam from each laser, while a photodiode (internal for the TOPTICA laser and external for the Newport laser) monitored output power. The main beam from the laser then passed through a mechanical chopper operating at 2 kHz before being injected into the chamber through a multi-mode 50 μm diameter fiber with a numerical aperture of 0.22.

Within the chamber, there were two optics aligned to a point within the plasma discharge. One was the injection lens, which had a 50 mm diameter and a focal length of 10 cm, mounted approximately 10 thruster diameters downstream. This lens focused the beam down to a 1 mm^3 spot size. We aligned the beam to channel centerline and injected it axially. The collection lens, which had a 75 mm diameter and a focal length of 20 cm, was oriented at an angle outside of the main plume of the thruster and aligned to the same spot as the injection lens.

Once fluoresced light from the transition was collected by the collection optic, it was sent through a multi-mode 1 mm diameter fiber with a numerical aperture of 0.39 to a bandpass filter to reduce noise. This light was then converted to current using a photomultiplier tube (PMT) and then to voltage using a transimpedance amplifier (TIA). Finally, we used a lock-in amplifier (LIA) tied to the frequency of the chopper to distinguish the fluorescence from the background light. We used an integration time of 300 ms on the LIAs. We power-corrected the measured signal by dividing it by the power input from the laser; this isolated the intensity of our fluorescence measurements from the intensity of the injection signal.

During operation, the thruster was mounted on a motion stage capable of translating axially such that the optical diagnostics could be kept stationary. For each condition, we performed axial LIF along channel centerline from approximately 0.13 thruster channel lengths L_{ch} upstream to 0.53 channel lengths downstream of the exit plane. This experimental domain is shown in figure 6.

Figure 7 shows an example of an ion velocity distribution function (IVDF) measured at $z = 1.53L_{ch}$ for krypton operation at 300 V and 15 A. The velocity resolution for this condition is approximately 200 m s^{-1} . There are two velocity populations that can be seen in this distribution, which has been shown to be typical of Hall thrusters [51, 55]. This has been attributed to the oscillatory nature of Hall thrusters and the time-averaged nature of our LIF measurements. In order to infer an average ion velocity from these profiles, we first performed a two-peak Gaussian fit at each location and then took the first moment. We estimated uncertainty in these averages through the bootstrapping method [56]. With this technique, we randomly sampled the raw IVDF trace and performed the same Gaussian fit to obtain a distribution of mean fitted velocities. We took the uncertainty to be a 95% confidence interval of the resulting distribution. The moments resulted in spatial profiles of average ion velocity along channel centerline.

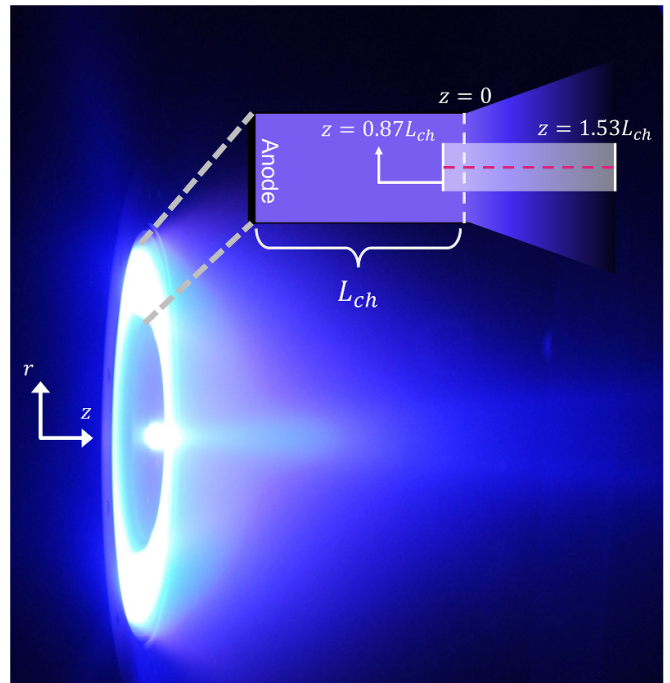


Figure 6. LIF interrogation domain (shown as a transparent rectangle) overlaid atop H9 operating on krypton at 300 V, 15 A. Channel centerline is represented by the dashed pink line.

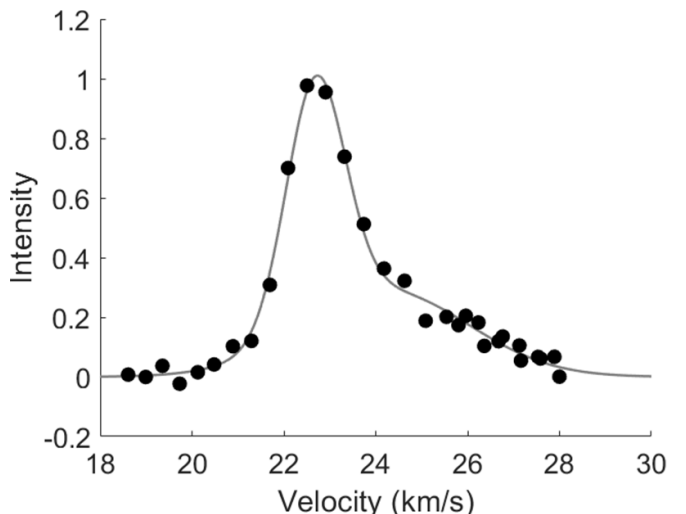


Figure 7. Measured (points) and two-peak Gaussian fit (line) ion velocity distribution function at $0.53L_{ch}$ downstream of the exit plane for H9 operating on krypton at 300 V, 15 A.

In this work, we neglect to account for broadening of the IVDF due to hyperfine and Zeeman splitting. We discount the former effect because it has been shown from previous LIF work performed on singly-charged xenon that it contributes less than 1% uncertainty to the velocity moment at the exit plane and downstream of the thruster channel [51, 57, 58]. We neglect the latter effect because it is symmetric, indicating that it should not impact our measurements of average ion velocity [51, 59].

Table 3. Experimentally measured thrust and anode efficiency for all conditions [9, 10].

Species	Condition	Thrust (mN)	η_a (%)
Xe	300 V, 15 A	292.9 ± 3.5	64.2 ± 1.6
Xe	400 V, 15 A	350.8 ± 3.4	66.5 ± 1.5
Xe	600 V, 15 A	447.2 ± 3.0	68.3 ± 1.3
Xe	300 V, 20 A	377.6 ± 3.8	64.2 ± 1.3
Xe	300 V, 30 A	547.0 ^a	—
Kr	300 V, 15 A	235.8 ± 2.5	52.2 ± 1.1
Kr	400 V, 15 A	269.1 ± 2.5	52.6 ± 1.1
Kr	600 V, 15 A	350.3 ± 2.5	54.7 ± 0.9
Kr	300 V, 20 A	317.3 ± 2.0	54.8 ± 0.8
Kr	300 V, 30 A	480.3 ^a	—

^a The 300 V, 30 A condition thrusts were linearly extrapolated from 15 to 20 A.

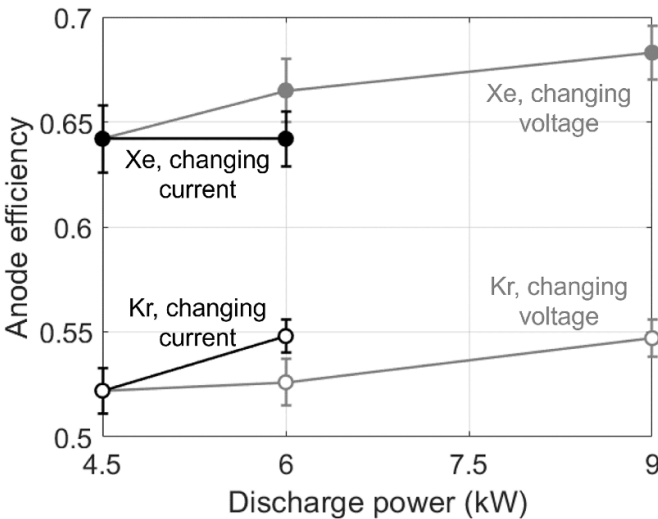


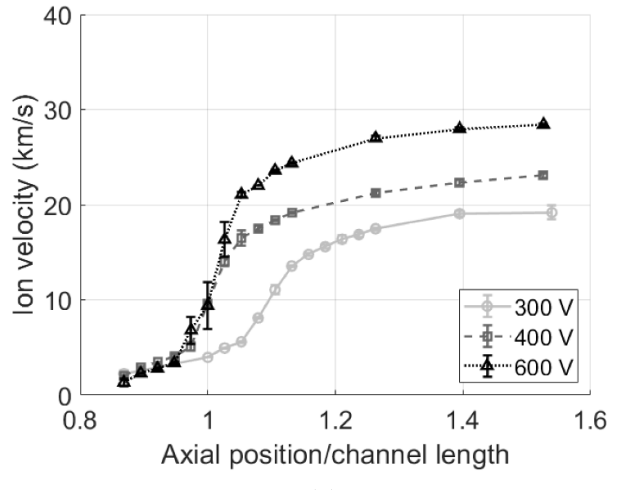
Figure 8. Experimentally measured anode efficiencies with increasing voltage and current held constant at 15 A (gray), and increasing current and voltage held constant at 300 V (black) for H9 operating on xenon and krypton.

4. Results

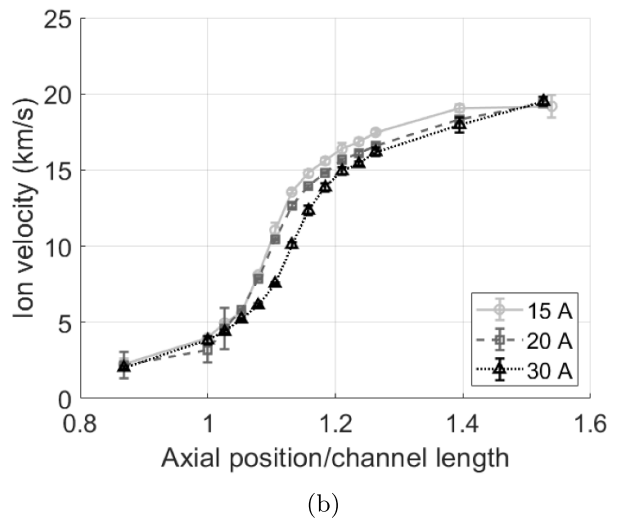
4.1. Experimental results

Here we summarize the global performance metrics for our thruster and present the ion velocity profiles obtained through LIF. The performance measurements have been previously published in references [9, 10] and are summarized in table 3. In figure 8, we show anode efficiency trends with increasing power. We note here that we did not have experimental thrust and anode efficiency measurements of the 30 A conditions. Instead, we estimated the values for those conditions by linearly extrapolating thrust from 15 to 20 A.

The thrust and efficiency results in table 3 and figure 8 show both metrics increasing monotonically with increasing power (both voltage and current). As we noted in our previous work [9], the efficiency gap between xenon and krypton remains approximately constant between the 300, 15 A and 600 V, 15 A conditions. This is in contrast to trends with increasing



(a)



(b)

Figure 9. Profiles of mean ion velocity along thruster channel centerline with xenon operation for (a) increasing discharge voltage with a constant discharge current of 15 A, and (b) increasing discharge current with a constant discharge voltage of 300 V.

voltage observed on unshielded thrusters where the efficiency gap closes [14, 15, 18]. On the other hand, we note that the gap decreases as current increases from 15 to 20 A with voltage held constant at 300 V. This is more in line with previous measurements on unshielded thrusters [13, 14, 16].

In figure 9, we show the ion velocity profiles for xenon operation at different voltages and currents. At higher voltages, the ions reach a faster final velocity due to the greater acceleration voltage. We also note that with increasing voltage, the profile moves upstream, consistent with previous measurements [48, 50, 60]. With increasing current, the final velocity remains approximately constant, and the acceleration region shifts downstream. This downstream shift in acceleration region is consistent with previous measurements on both unshielded [48] and shielded [50, 60, 61] thrusters.

In figure 10, we present the velocity profiles for krypton as a function of voltage and current. We first note that krypton

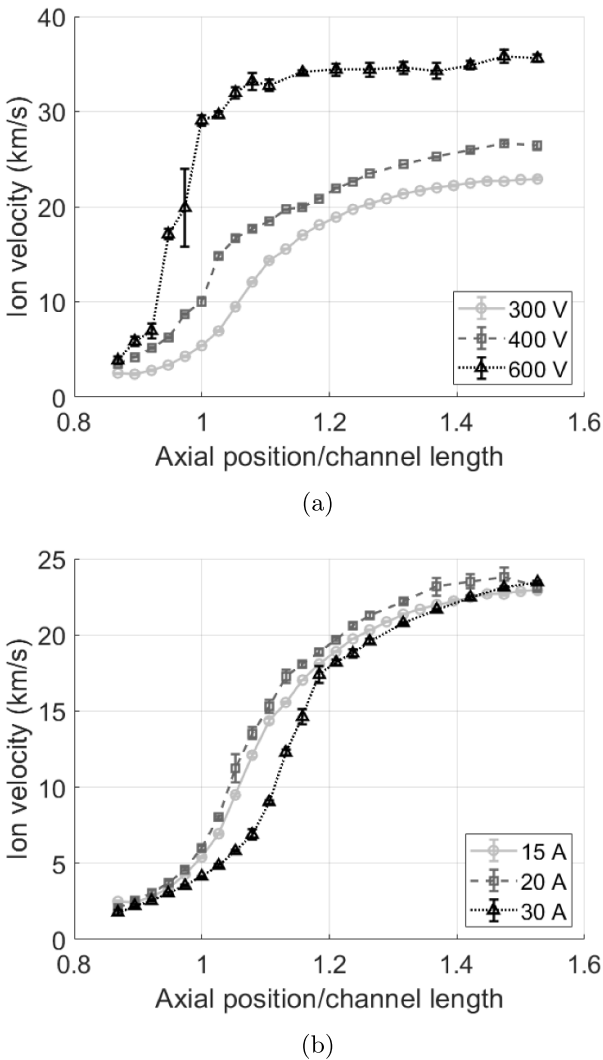


Figure 10. Profiles of mean ion velocity along thruster channel centerline with krypton operation for (a) increasing discharge voltage with a constant discharge current of 15 A, and (b) increasing discharge current with a constant discharge voltage of 300 V.

reaches a higher final velocity than xenon at the same operating condition. This stems from the fact that krypton is a lighter gas and therefore achieves a faster final velocity for a given acceleration voltage. In terms of trends with voltage, the velocity profiles exhibit similar behavior to xenon in that they generally move upstream and steepen. With increasing current, there is a similar downstream shift in the acceleration region for krypton operation as exhibited by the thruster operating on xenon from 15 to 30 A.

4.2. Simulation results

We present in this section the results from our calibrated simulations, highlighting the metrics that illustrate acceptable agreement with experimental data and using average values of internal plasma properties to observe trends in mass utilization.

Table 4. Simulated values of thrust, anode efficiency, and integrated velocity residual for all conditions.

Species	Condition	Thrust (mN)	η_a (%)	IVR
Xe	300 V, 15 A	291.7	63.9	0.07
Xe	400 V, 15 A	349.3	66.0	0.11
Xe	600 V, 15 A	450.7	69.2	0.08
Xe	300 V, 20 A	377.4	64.2	0.09
Xe	300 V, 30 A	543.2	64.7	0.08
Kr	300 V, 15 A	236.8	52.8	0.07
Kr	400 V, 15 A	270.7	53.1	0.05
Kr	600 V, 15 A	352.9	55.3	0.41 ^a
Kr	600 V, 15 A	382.8 ^b	65.0 ^b	0.10
Kr	300 V, 20 A	318.6	55.3	0.05
Kr	300 V, 30 A	477.6	60.6	0.07

^a This condition did not meet the IVR requirement.

^b This condition did not meet the thrust and efficiency requirements.

4.2.1. Demonstrating model calibration. In the interest of brevity, we show the calibrated anomalous collision frequency profiles and simulated ion velocity profiles for all conditions in the [appendix](#). We summarize key global metrics (section 3.2.3) from these simulations in table 4, where we compare the simulation thrust, anode efficiency, and ion velocity residual (equation (10)) for each condition. In comparing to table 3, all conditions satisfy our criteria outlined in section 3.2.3 with two exceptions. First, we again note that there was no thrust data experimentally measured at 30 A. For these two simulation cases, we neglected condition (iii) and modified condition (ii) from section 3.2.3 such that we matched the extrapolated thrust of the 30 A condition to within 1%, approximately equal to the standard experimental error. Second, we were not able to satisfy all calibration requirements for krypton at 600 V, 15 A. We could reliably produce a profile that satisfied the thrust and efficiency requirement but had a high IVR ($IVR > 0.4$) and another profile that matched the velocity profile ($IVR = 0.1$) but had a thrust 30 mN too high. We show both values for performance metrics in table 4 and both ion velocity profiles in section 3.3.2. We suspect our inability to satisfy the criteria may be due to the simplified form of the anomalous collision frequency profile that we have adopted, which makes it difficult for the simulated ion velocity profile to capture the steepness of the experimentally measured profile. Additionally, the intense ($>100\%$) oscillations at this operating condition [9] may lead to the time-averaged IVDF containing multiple ion populations. To account for our lack of convergence to an exact match, we consider both profiles in the following analysis.

4.2.2. Averaged 1D profiles of plasma properties. We show in figure 11 examples of radially-averaged 1D simulated profiles of key plasma properties in the axial direction. To obtain these profiles, we averaged each parameter radially across the channel at each axial location, yielding a 1D profile from this 2D data in the z - r plane. The parameters we evaluated were plasma density n_e , electron temperature T_e , ionization rate coefficient k_{iz} , and neutral velocity v_n . While we only show

profiles for the 300 V, 15 A conditions, the trends are broadly representative for all cases.

We can see from figure 11(a) that the electron temperature steadily increases through the region before peaking slightly downstream of the exit plane and subsequently decreasing. We can attribute the increase in temperature as the electrons transit upstream from 1.5 to $1.1L_{ch}$ to Ohmic heating. We expect the temperature to peak at the location of strongest magnetic field where the electrons are most strongly impeded [62]. The subsequent decrease in temperature from the exit plane to the anode can be attributed to ionization and wall losses. The electron temperature peaks at about 40 eV for both propellants, a scaling of approximately $T_e \propto 0.13V_d$. This is a departure from the assumption of $T_e \propto 0.2V_d$ we made in our previous work on shielded thrusters [9] and is closer to the scaling of $T_e \propto 0.1V_d$ exhibited by unshielded thrusters [28, 63–66]. Physically, this relationship arises from the fact that the discharge voltage is the source for electron heating. We also note that the electron temperature of krypton is slightly higher than that of xenon throughout the range, in keeping with trends previously seen on unshielded thrusters [11, 67]. This may be attributed to the need for hotter temperatures while running on krypton to maintain ion production in the thruster, which in turn may be the result of krypton's lower ionization rate coefficient at a given temperature (figure 2).

The profiles of ionization rate coefficient, shown in figure 11(b), trend in the same manner as electron temperature. However, the ionization rate coefficient of xenon is higher than krypton throughout the channel. This is because the slightly higher electron temperatures of krypton are not enough to make up for the difference in ionization rate coefficient as seen in figure 2. This behavior is in line with our previous attribution of krypton's lower mass utilization to its lower ionization rate coefficient at a given temperature [9].

Figure 11(c) shows that the plasma density for both propellants increases immediately downstream of the anode before decaying throughout the rest of the channel. This behavior can be understood by again considering the movement of electrons towards the upstream anode. The density increases from the exit plane (at L_{ch}) to $0.1L_{ch}$ due to ionization and subsequently decreases from $0.1L_{ch}$ to the anode due to the existence of pre-sheath effects directly downstream of the anode. We also note that the peak plasma density of xenon is approximately a factor of two higher than that of krypton. This is likely due to krypton's higher mobility—because of its lower mass, krypton reaches higher velocities at a given discharge voltage than xenon (cf figures 9(b) and 10(b)). Since the krypton population is moving faster while a constant current is being maintained, particles spend less time in a given region, leading to a lower particle density.

Finally, we see in figure 11(d) that the neutral velocity gradually increases through the channel before plateauing near the exit plane at L_{ch} . This behavior has been attributed to the expansion of the gas as it exits from the anode, selective ionization that preferentially depletes slower neutrals, and recombination of ions at the channel walls [29]. This accelerating

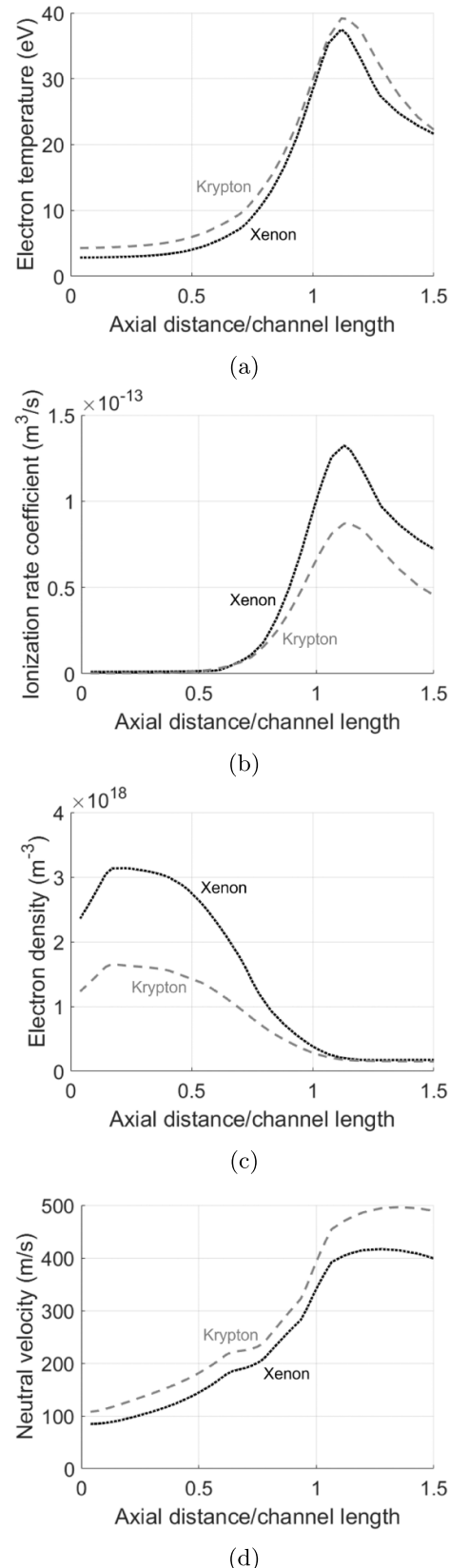


Figure 11. Radially-averaged axial profiles of (a) electron temperature, (b) ionization rate coefficient, (c) plasma density, and (d) neutral velocity for operation at 300 V, 15 A on xenon and krypton.

behavior has been observed in experimental measurements of neutral xenon velocity within the channel of a Hall thruster [29, 58, 68], and the magnitudes are consistent with what has been measured on the same or similar thrusters [58, 68]. We also see that krypton's neutral velocity is higher than xenon's, again owing to its lower mass.

4.2.3. Spatially averaged plasma properties. While the radially-averaged 1D profiles of plasma properties are useful for understanding changes through the channel, volumetrically-averaged (0D) values allow us to use the framework outlined in section 2 to understand how the mass utilization scales. To this end, we define an average value of a given property x over the axial direction z as

$$\langle x \rangle = \frac{\int_0^L x(z) dz}{L}, \quad (11)$$

where $z = 0$ is the location of the anode and $z = L$ is the length of integration. We computed the integral using trapezoidal numerical integration. For this work we used $L = 1.5L_{ch}$ as we found this to be the location at which for all conditions the neutral density has decayed to near-zero, implying that the bulk of the ionization is complete. For the krypton 600 V, 15 A condition (see section 4.2.1), we evaluated equation (11) for both cases and averaged them, evaluating uncertainty as the difference between cases. Armed with this framework for analyzing the outputs of our simulation, we present here our 0D results as a function of increasing discharge voltage and current for each propellant.

In figure 12(a), we see that the spatially averaged electron temperature steadily increases with discharge voltage. The electron temperature of krypton is 2–3 eV higher than that of xenon at all voltages. The scaling of electron temperature with voltage is expected from a consideration of energy balance [28]. As shown in figure 12(b), the electron temperature remains nearly constant with increasing current. With the exception of a slightly-higher electron temperature of 18 eV for krypton at 15 A, all other average electron temperatures for both propellants are ~ 15 eV.

In figure 13 we plot the trends in averaged ionization rate coefficient for increasing voltage and current. While the trends with power closely mirror those of electron temperature (figure 12), the ionization rate of xenon is higher than krypton's at all conditions due to its lower ionization energy. For both gases, however, the ionization rate increases with voltage and has very little variation with current.

From figure 14, we can see that the plasma density increases with both voltage and current, although the increase with voltage is less dramatic than with current. The higher plasma density with current is intuitive—as more neutrals flow into the channel, more charge carriers are made available, and the plasma density increases. The dependence on voltage, however, is not expected based on conventional scaling laws. For a constant current and the higher velocities at increased voltages, we might anticipate that the plasma density decreases due to continuity. This behavior is not reflected here. We comment further on this in section 5.2. We also note that at all

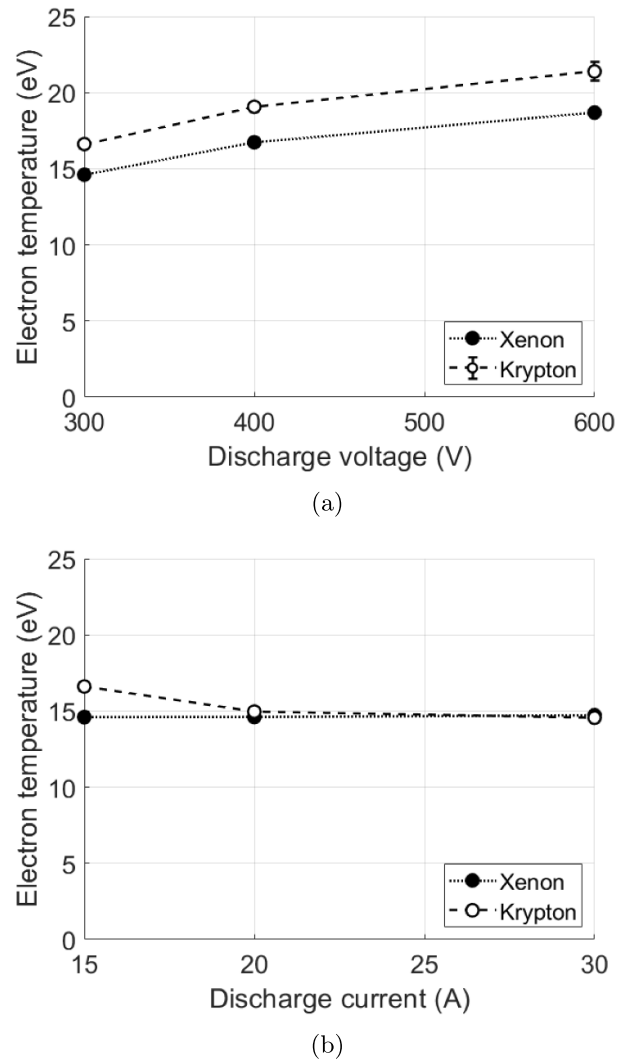
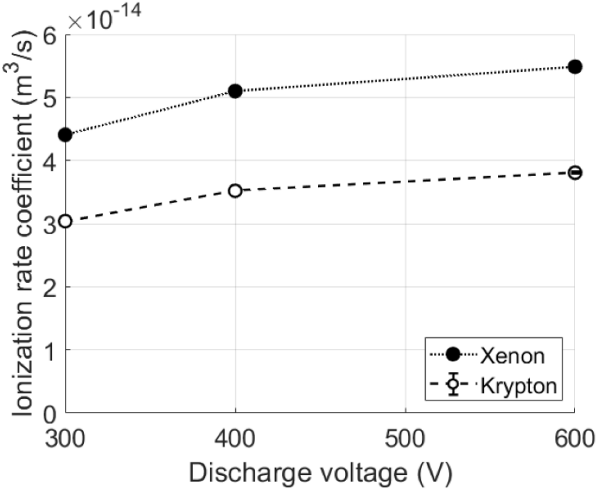


Figure 12. Average electron temperature in channel of xenon and krypton operation for (a) increasing discharge voltage with a constant discharge current of 15 A, and (b) increasing discharge current with a constant discharge voltage of 300 V.

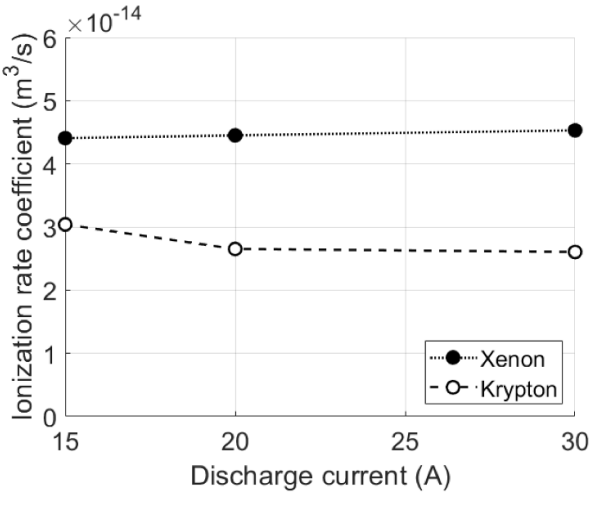
conditions, xenon's plasma density is $\sim 50\%–90\%$ higher than krypton's.

We do not show plots for the channel-averaged neutral velocity at all conditions because we found that this value varied by less than $\sim 4\%$ across all conditions (voltage and current) for a given propellant. This is to be expected given our prescribed constant inlet temperature at the anode. The channel-averaged neutral velocity was approximately 238 m s^{-1} for xenon and 287 m s^{-1} for krypton across all conditions.

4.2.4. Mass efficiency. We present in figure 15 the theoretical, simulated, and experimental values of mass utilization. The theoretical values are calculated by evaluating equation (6) with the 0D plasma properties presented in the previous section. In all cases, we used a value of $\alpha = 0.25$ and ionization region of $L = 1.5L_{ch}$ to achieve the best agreement with experimental measurements of mass utilization. We



(a)

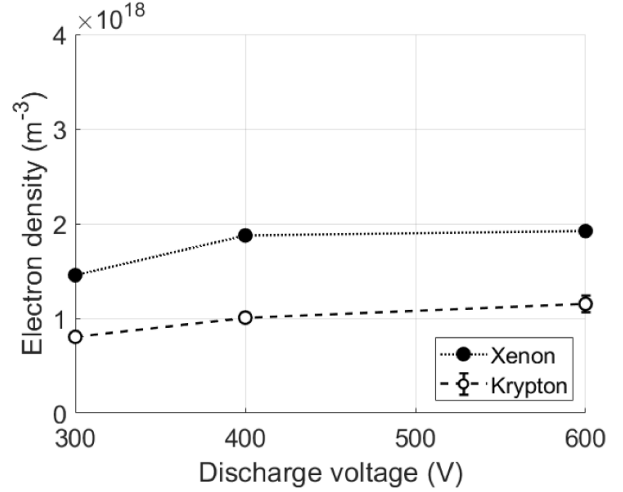


(b)

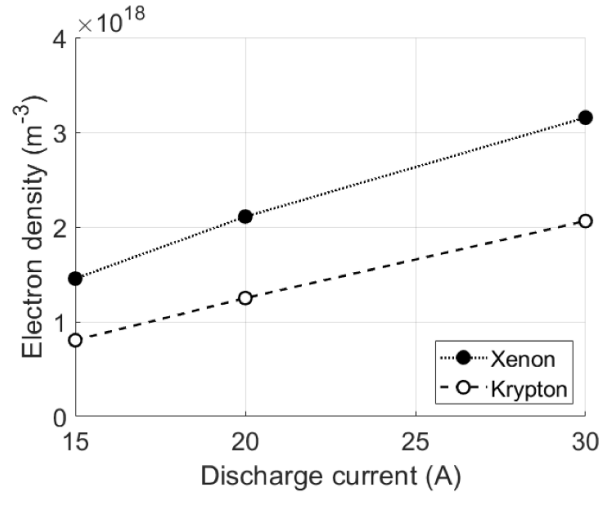
Figure 13. Average ionization rate coefficient in channel of xenon and krypton operation for (a) increasing discharge voltage with a constant discharge current of 15 A, and (b) increasing discharge current with a constant discharge voltage of 300 V.

can compute the simulated mass utilization efficiencies from Hall2De directly by integrating the ion mass flow rate along the outflow boundaries and dividing by the input mass flow rate. However, the complex nonlinear physics governing Hall thrusters make extracting physical intuition from these simulated values different. Our simplified physical model, while not as high fidelity as the Hall2De simulation, captures the majority of the important physics governing mass utilization and is therefore a useful tool for assessing the relative performance of xenon and krypton. The experimental values shown at the lower-power conditions are from reference [9]. While the values and trends exhibited by the efficiencies are not in exact agreement, they all support the overall behavior of the efficiency gap closing with both increasing voltage and current.

Figure 15 qualitatively shows that mass efficiency as calculated with our model (equation (6)) increases with both voltage and current. This is consistent with the theory we



(a)



(b)

Figure 14. Average plasma density in channel of xenon and krypton operation for (a) increasing discharge voltage with a constant discharge current of 15 A, and (b) increasing discharge current with a constant discharge voltage of 300 V.

outlined in section 2 and with previous work on Hall thrusters. Using this theoretical framework allows us to identify which plasma parameters are driving the increases in mass utilization. With voltage, the increases in both electron temperature (figure 12(a)) and plasma density (figure 14(a)) serve to decrease the ionization mean free path. With current, only the higher plasma density (figure 14(b)) drives a shorter ionization mean free path. At all conditions, we see that the mass utilization of xenon is higher than that of krypton. This result is consistent with our previous experimental measurements of mass utilization and numerous other Hall thruster studies. As we discuss in the following section 5, the key driver of this efficiency gap is xenon's higher average plasma density and ionization rate coefficient in all cases. We note that following the scaling of the theoretical model, the efficiency gap closes at higher powers for both voltage and current, i.e. krypton's mass utilization improves more than xenon's. This finding is in

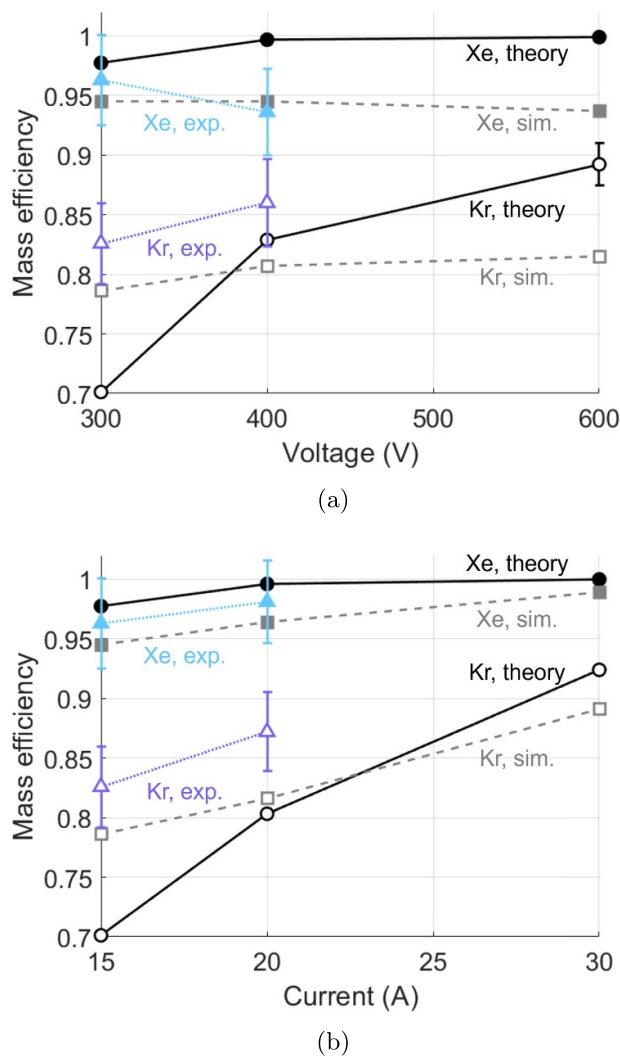


Figure 15. Mass efficiencies of xenon and krypton operation as calculated from theory with simulated plasma parameters via equation (6) (black solid line), as output from Hall2De simulation (gray dashed line), and as experimentally measured (colored dotted line). Values are shown for (a) increasing discharge voltage with a constant discharge current of 15 A, and (b) increasing discharge current with a constant discharge voltage of 300 V.

contrast to the experimentally-observed *anode* efficiency gap between xenon and krypton, which was shown to not close at high voltages (figure 8). This discrepancy is likely attributed to the fact that there are more contributors to the anode efficiency than just mass utilization, a point we return to in section 5.2.

Ultimately, the efficiency gap closes at high powers because of the exponential dependence of mass utilization (equation (6)). Xenon, which has a higher plasma density at lower powers than krypton, exhibits a mass utilization closer to the asymptotic 100% even at its lowest-power condition. Therefore, as the ionization mean free path decreases, xenon's mass utilization shows a smaller increase compared to krypton.

5. Discussion

In this section, we elaborate on the differences in mass utilization between xenon and krypton as well as trends in plasma parameters with increasing power. We discuss these trends in context of how they relate to the behavior of the efficiency gap between these propellants at high voltages and high currents.

5.1. Overall efficiency comparison

A key finding from our analysis is that, as expected, the mass utilization is higher for xenon than it is for krypton at all conditions. This is broadly consistent with multiple previous studies [9, 11–17]. In these previous works, the cause for the difference in efficiency was largely attributed to the role of ionization rate [9, 13, 17, 18, 69, 70]. Assuming that xenon and krypton have the same electron temperature at a given condition, xenon would have a higher ionization rate coefficient (figure 2). While we did find this to be the case (figure 11(b)), we also found that xenon has a significantly higher plasma density than krypton (figure 11(c)). The implication of this result is that xenon's higher mass utilization cannot be solely attributed to its higher ionization rate; instead, xenon's higher plasma density, lower neutral velocity, and higher ionization rate must all be taken into consideration.

5.2. Efficiency trends with increasing voltage

Figure 15(a) shows that the mass utilization increases with voltage for both propellants. This can be attributed to both higher plasma densities (figure 14(a)) and ionization rate coefficients (figure 13(a)). The influence of ionization rate is not surprising given the known scaling between voltage and electron temperature [28, 63–66]. The trend in average density with voltage also likely can be attributed to increasing ionization rate with temperature and voltage. Indeed, as we show in figure 16(a), although plasma density in the region downstream of the exit plane decreases at high voltage (a consequence of ion current continuity in the channel), the density from the anode to $\sim 0.2L_{ch}$ upstream of the exit plane increases with voltage. This result is likely linked to higher ionization rates (figure 16(c)) due to slight increases in temperature with voltage in this region (figure 16(b)). The higher densities in this upstream region ultimately dominate when averaging over our axial range of interest. Thus, in practice, the increase in ionization rate drives the trends in voltages—both directly through the average value and indirectly through inducing high charge production in the upstream ionization region.

These arguments ultimately lead us to reconsider our previously reported conclusions about the disparity in performance trends with voltage of magnetically shielded and unshielded thrusters on krypton and xenon. In our previous work [9], we had assumed that krypton and xenon would both have the same average temperature for a given discharge voltage. We also argued that the electron temperatures in shielded thrusters are higher than in unshielded. Due to the nonlinear nature of

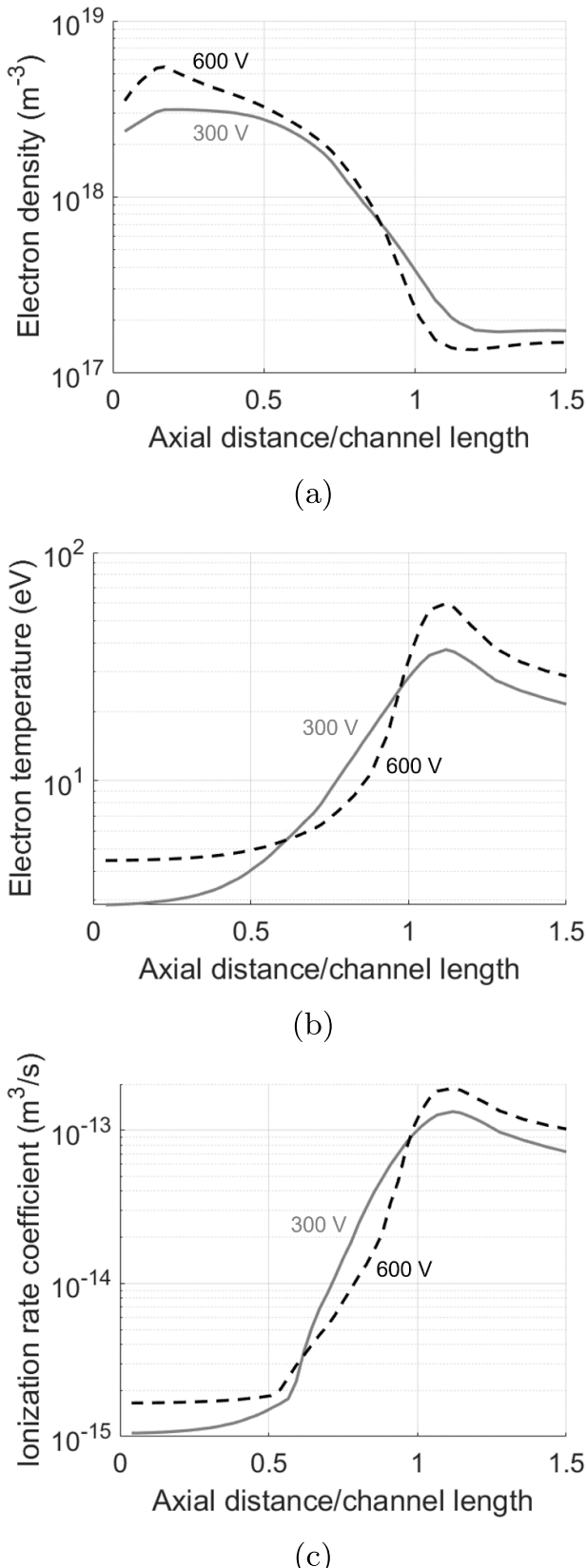


Figure 16. Axial profiles of (a) plasma density, (b) electron temperature, and (c) ionization rate coefficient along channel centerline for operation at 300 V, 15 A (gray) and 600 V, 15 A (black) on xenon.

the ionization rate coefficients for each gas, we showed in this previous work that the stronger dependence of temperature on voltage with shielded thrusters could explain why the gap in mass utilization seen when operating with xenon versus krypton does not close with voltage in the same way that it does for unshielded thrusters.

Our current work suggests that our key assumption—the scaling factor of electron temperature on shielded thrusters—is invalid. This thus invites the question as to why the efficiency gap does not close. Indeed, our mass utilization results would actually suggest that the efficiency gap *should* close in the same way as been observed on unshielded thrusters [14, 15, 18]. Ultimately, this behavior stems from the fact that mass utilization has an exponential dependence on ionization rate coefficient and plasma density. The significantly higher plasma density and ionization rate coefficient of xenon means that even at the lowest-power conditions, its mass utilization is near the asymptote of 100%. Krypton, on the other hand, starts at lower mass utilization and therefore benefits from the nonlinear scaling of this parameter, exhibiting more rapid improvement when contrasted with xenon. We expand upon this behavior in section 5.3.

The fact that our theoretical results show the mass utilization gap narrowing suggests we need to reconsider the effect of other efficiency losses beyond mass utilization. For example, as we have noted in our previous work [9], the second largest driver of the performance gap between xenon and krypton is the divergence efficiency. In light of the fact that changing from an unshielded to a shielded topology pushes the acceleration region downstream and increases divergence [62], it is possible that the acceleration region and therefore plume divergence may respond differently at higher voltages and for each propellant. While a discussion of these effects are outside the scope of the analysis presented in this paper, we remark that our work— informed by experimentally-validated simulation—has at least eliminated one candidate explanation for the different observed behaviors in shielded versus unshielded thrusters.

5.3. Efficiency trends with increasing current

Figure 17 illustrates qualitatively why the mass utilization curve improves more rapidly with current for krypton than xenon. In this case, we have plotted the expected mass efficiency as a function of plasma density. We have again used a factor of $\alpha = 0.25$ and ionization length of $L = 1.5L_{\text{ch}}$. We also assumed rate coefficients and neutral velocities for each propellant by averaging over all three current conditions. These values are $4.5 \times 10^{-14} \text{ m}^3 \text{ s}^{-1}$ and 238 m s^{-1} respectively for xenon, and $2.8 \times 10^{-14} \text{ m}^3 \text{ s}^{-1}$ and 287 m s^{-1} for krypton. This is justified given the relatively small variation in this parameter for both gases with voltage (figure 13(b)). As can be seen from figure 17, the mass utilization increases nonlinearly and eventually asymptotes with increasing plasma density for both cases, reflecting a state in which complete ionization of the input neutrals occurs.

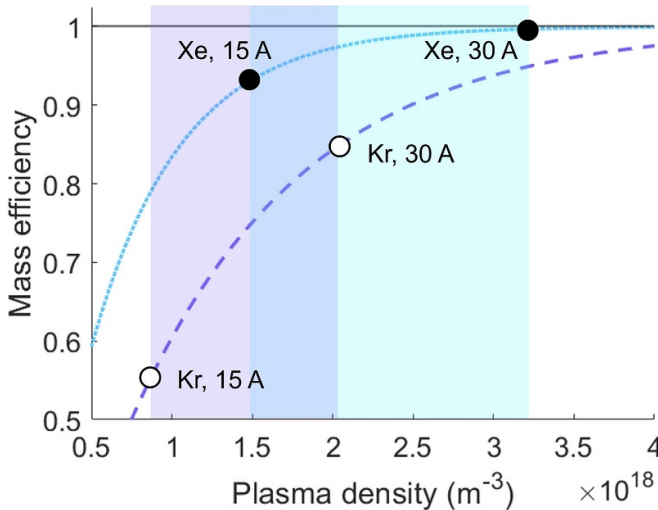


Figure 17. Notional mass efficiency scaling for xenon (blue dotted) and krypton (purple dashed), with 15 A and 30 A conditions shown with circular markers for xenon (filled) and krypton (open).

Figure 15(b) shows that the mass utilization increases for both propellants with discharge current at fixed voltage, but the relative increase for krypton ($\sim 30\%$ from 15 to 30 A) exceeds that of xenon ($< 10\%$ from 15 to 30 A). The improvement in utilization for both gases with current largely can be explained by the plasma density. Indeed, while the ionization rate coefficient remains nearly constant for a given propellant, the average plasma density for both xenon and krypton increases by a factor between 2.2 and 2.5 from 15 to 30 A (figure 14(b)).

In practice, at a given current, the xenon case has a higher plasma density than krypton. This fact, combined with the lower neutral velocity and higher ionization rate coefficient of xenon, serves to place the mass utilization for xenon closer to the asymptote in mass utilization at the 15 A condition. The subsequent increase in plasma density with xenon from increasing current thus has only an incremental improvement in overall mass efficiency. On the other hand, the lower density of krypton at 15 A combined with this propellant's higher speed and lower ionization rate both serve to place the initial mass utilization at a lower value. The mass utilization thus improves markedly with increasing current and density.

In light of this description, we would anticipate that the performance gap decreases with increasing current. This behavior is reflected by our experimental observations in our previous work [22] where we observed that the overall efficiency gap between propellants did close with current. With that said, we cannot definitively claim that this trend in mass utilization is the only factor that influences trends in overall efficiency. Indeed, per our discussion in the previous section,

other efficiency modes may change on shielded thrusters and influence behavior with increasing current.

6. Conclusion

In this work, we have investigated the mass utilization efficiency of a magnetically shielded Hall thruster as a function of discharge voltage and current for both xenon and krypton propellants. We leveraged experimental measurements and calibrated simulations to infer trends in mass utilization as well as the plasma properties inside the thruster channel driving these trends.

We found that the mass utilization improves with both voltage and current for both gases. We interpreted the driving factors for these trends in the context of a 0D equation for mass utilization evaluated with volumetrically-averaged plasma properties from the channel given by our calibrated simulations. This analysis led to the conclusion that the improvement in mass utilization with voltage can be attributed to increases in both the ionization rate and plasma density in the channel, both of which are the result of higher electron temperature with discharge voltage. The observed increase in mass utilization with current density stems primarily from markedly higher plasma densities.

Our results also showed that the relative gap between mass utilization for krypton and xenon should close with both voltage and current. This can be attributed to the fact that the mass utilization is a nonlinear function of plasma density and neutral velocity that asymptotically approaches unity. At a given operating condition, xenon has a higher initial density than krypton and thus is closer to 100% mass utilization. The return in mass efficiency improvement with increasing power for xenon is therefore not as marked as the trend exhibited by krypton.

We have remarked that although the mass utilization gap between gases closes with current and voltage, we have found experimentally that the disparity in overall thruster efficiency does not decrease with voltage for a shielded thruster [9]. This is a departure from previously measured trends in the overall efficiency gap with voltage for unshielded thrusters. While we have previously attributed this disparity to a different response of mass utilization between shielded and unshielded thrusters, our results suggest that this is not the case. Instead, other efficiency modes may be driving this trend, such as changes in how divergence angle responds to voltage in shielded versus unshielded thrusters. In contrast, the overall efficiency gap between propellants does close with current as measured experimentally, which in light of our results, is predominantly driven by mass utilization.

In summary, the findings in this work represent a comprehensive investigation into the physical processes underlying

the response of mass utilization of magnetically shielded thrusters operating on xenon and krypton to changing power levels. Given the growing interest in alternative propellants like krypton, these key experimental results and subsequent insights may be important considerations for informing the optimization of the next-generation of long-life high-power thrusters.

Data availability statement

All data that support the findings of this study are included within the article (and any supplementary files).

Acknowledgments

The authors would like to acknowledge Dr Ioannis Mikellides and Dr Alejandro Lopez Ortega of the Jet Propulsion Laboratory for their guidance with Hall2De. The authors also would like acknowledge Mr Parker Roberts and Dr Matthew Byrne for assistance in data collection and analysis. This research was supported in part through computational resources and services provided by Advanced Research Computing at the University of Michigan, Ann Arbor.

Appendix. Calibrated Simulations

In this section, we show the anomalous transport profiles along channel centerline found by calibrating all conditions, as well as the simulation-generated velocity profiles.

In figure 18, we show the calibrated anomalous transport profiles along channel centerline for xenon with increasing voltage and increasing current.

In figure 19, we show the calibrated anomalous transport profiles for krypton with increasing voltage and increasing current.

In figure 20, we show all ten cases of velocity profiles from simulation compared to experimental data.

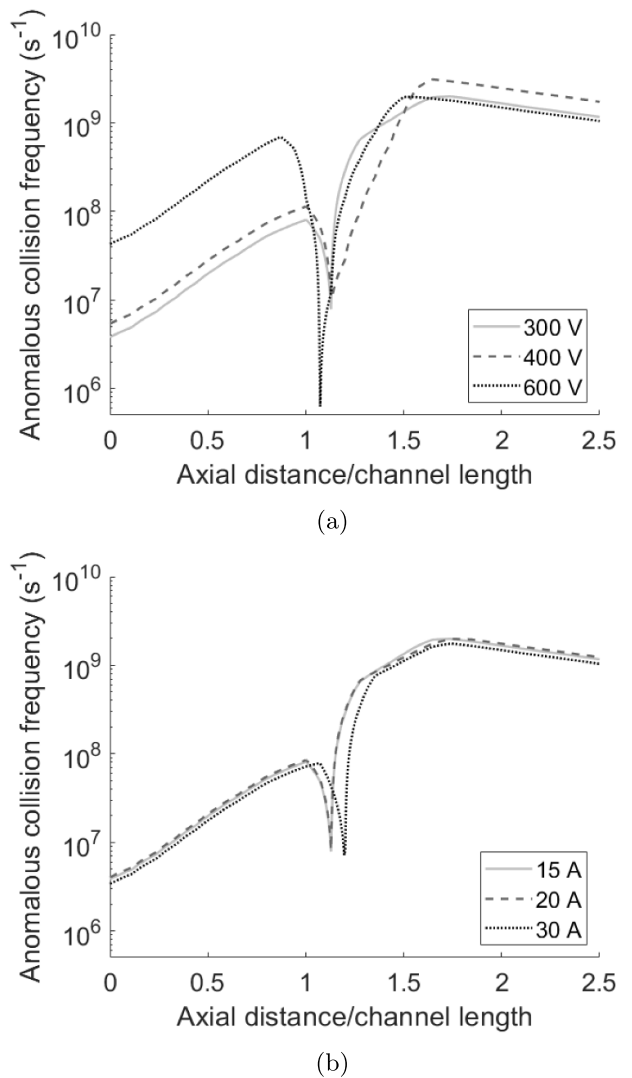


Figure 18. Calibrated anomalous electron collision frequency profiles along thruster channel centerline with xenon operation for (a) increasing discharge current with a constant discharge voltage of 300 V, and (b) increasing discharge voltage with a constant discharge current of 15 A.

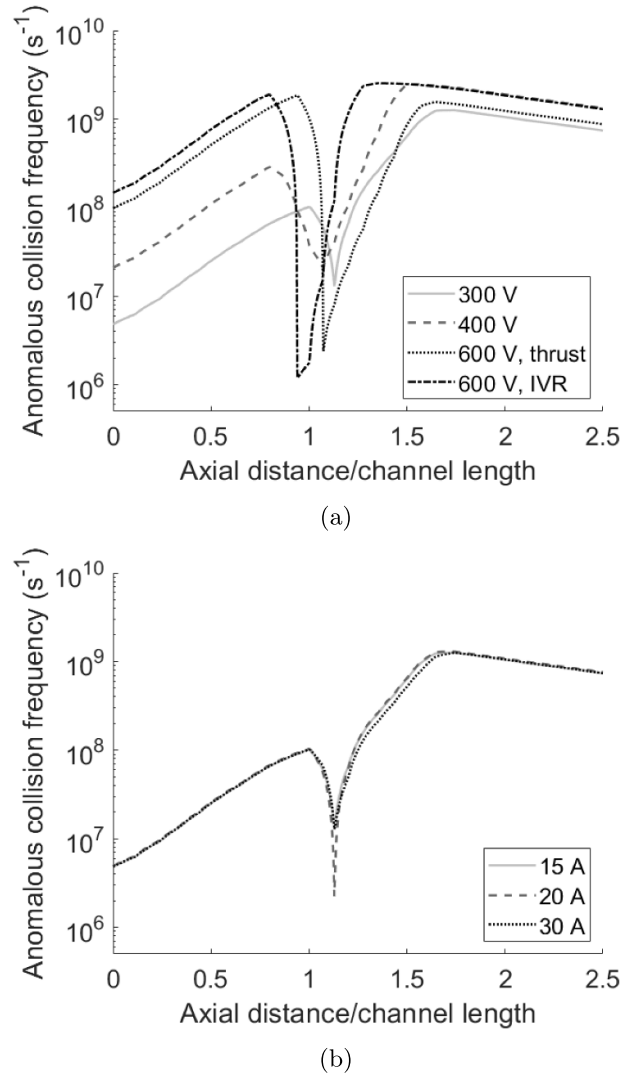


Figure 19. Calibrated anomalous electron collision frequency profiles along thruster channel centerline with krypton operation for (a) increasing discharge voltage with a constant discharge current of 15 A, and (b) increasing discharge current with a constant discharge voltage of 300 V.

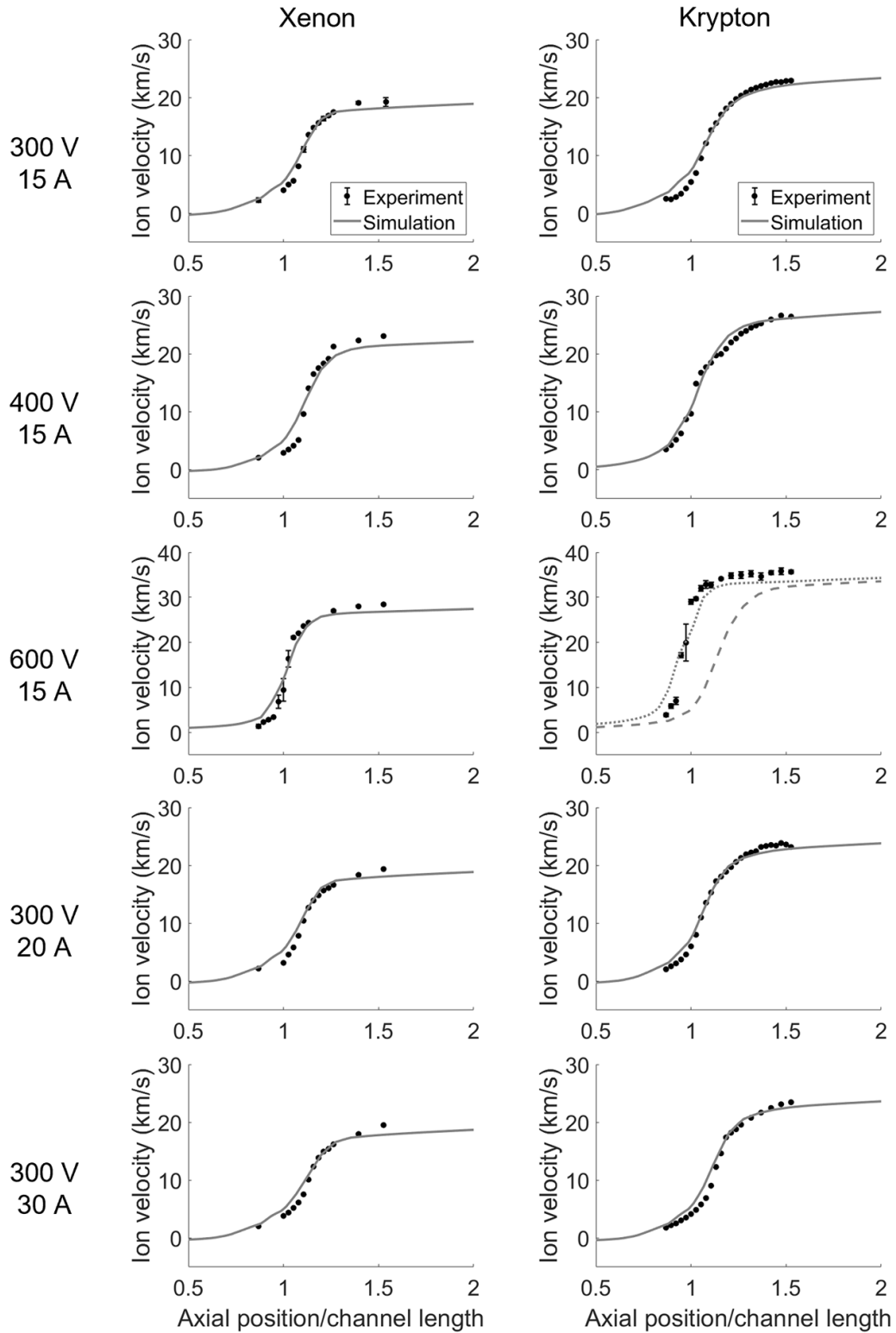


Figure 20. Experimental (black) and simulation (gray) ion velocity profiles along thruster channel centerline for each condition. Note that the 600 V, 15 A conditions have a different scale for ion velocity due to the high voltage. For the krypton 600 V, 15 A condition, the dashed line is the condition at which the thrust/efficiency matched and the dotted line is the condition at which the IVR matched.

ORCID iDs

- Leanne L Su  <https://orcid.org/0000-0002-7859-6807>
 Thomas A Marks  <https://orcid.org/0000-0003-3614-6127>
 Benjamin A Jorns  <https://orcid.org/0000-0001-9296-2044>

References

- [1] Oh D Y *et al* 2019 Development of the Psyche mission for NASA's discovery program *Int. Electric Propulsion Conf.*
- [2] Snyder J S, Chaplin V H, Goebel D M, Hofer R R, Lopez Ortega A, Mikellides I G, Kerl T, Lenguito G, Aghazadeh F and Johnson I 2020 Electric propulsion for the Psyche mission: development activities and status *AIAA Propulsion and Energy 2020 Forum* p 3607
- [3] Bapat A, Salunkhe P B and Patil A V 2022 Hall-effect thrusters for deep-space missions: a review *IEEE Trans. Plasma Sci.* **50** 189–202
- [4] Mikellides I G, Katz I, Hofer R R and Goebel D M 2014 Magnetic shielding of a laboratory Hall thruster. I. Theory and validation *J. Appl. Phys.* **115** 043303
- [5] Hofer R R, Goebel D M, Mikellides I G and Katz I 2014 Magnetic shielding of a laboratory Hall thruster. II. Experiments *J. Appl. Phys.* **115** 043304
- [6] The Economist 2023 How rare-gas supply adapted to Russia's war (available at: www.economist.com/finance-and-economics/2023/03/30/how-rare-gas-supply-adapted-to-russias-war)
- [7] Foust J 2023 SpaceX launches first upgraded Starlink satellites (available at: <https://spacenews.com/spacex-launches-first-upgraded-starlink-satellites/>)
- [8] Szabo J, Pote B, Paintal S, Robin M, Hillier A, Branam R D and Huffmann R E 2012 Performance evaluation of an iodine-vapor Hall thruster *J. Propuls. Power* **28** 848–57
- [9] Su L L and Jorns B A 2021 Performance comparison of a 9-kW magnetically shielded Hall thruster operating on xenon and krypton *J. Appl. Phys.* **130** 163306
- [10] Su L L and Jorns B A 2023 Erratum: "Performance comparison of a 9-kW magnetically shielded Hall thruster operating on xenon and krypton" (*J. Appl. Phys.* 130, 163306 (2021)) *J. Appl. Phys.* **134** 169901
- [11] Bugrova A, Bishnev A, Desyatkov A, Kozintseva M, Lipatov A and Dudeck M 2013 Experimental investigations of a krypton stationary plasma thruster *Int. J. Aerosp. Eng.* **2013** 686132
- [12] Kurzyna J, Jakubczak M, Szelecka A and Dannenmayer K 2018 Performance tests of IPPLM's krypton Hall thruster *Laser Part. Beams* **36** 105–14
- [13] Linnell J A and Gallimore A D 2006 Efficiency analysis of a Hall thruster operating with krypton and xenon *J. Propuls. Power* **22** 1402–18
- [14] Kamhawi H, Haag T, Jacobson D and Manzella D 2011 Performance evaluation of the NASA-300M 20 kW Hall thruster *47th Joint Propulsion Conf. and Exhibit* (San Diego, CA) (American Institute of Aeronautics and Astronautics) (<https://doi.org/10.2514/6.2011-5521>)
- [15] Peterson P, Jacobson D, Manzella D and John J 2005 The performance and wear characterization of a high-power high-Isp NASA Hall thruster *41st Joint Propulsion Conf. and Exhibit* (Tucson, AZ) (American Institute of Aeronautics and Astronautics) (<https://doi.org/10.2514/6.2005-4243>)
- [16] Marrese C, Gallimore A D, Haas J, Foster J, King B, Wook Kim S and Khartov S 1995 An investigation of stationary plasma thruster performance with krypton propellant
- [17] Jacobson D T and Manzella D H 2003 50 kW class krypton Hall thruster performance *39th Joint Propulsion Conf. and Exhibit* (Huntsville, Alabama) (NASA) (<https://doi.org/10.2514/6.1995-2932>)
- [18] Hofer R R, Peterson P Y, Jacobson D T and Manzella D M 2004 Factors affecting the efficiency of krypton Hall thrusters *46th Meeting of the APS Division of Plasma Physics* (Savannah, GA)
- [19] Cusson S E, Hofer R R, Lobbia R, Jorns B A and Gallimore A D 2017 Performance of the H9 magnetically shielded Hall thrusters *35th Int. Electric Propulsion Conf.* (Atlanta, Georgia)
- [20] Vincent B, Tsikata S and Mazouffre S 2020 Incoherent Thomson scattering measurements of electron properties in a conventional and magnetically-shielded Hall thruster *Plasma Sources Sci. Technol.* **29** 035015
- [21] Su L L *et al* 2023 Operation and performance of a magnetically shielded Hall thruster at ultrahigh current densities on xenon and krypton *AIAA SCITECH 2023 Forum* (National Harbor, MD) p 0842
- [22] Su L L, Roberts P J, Gill T, Hurley W, Marks T A, Sercel C L, Allen M, Whittaker C B, Viges E and Jorns B A 2024 High-current density performance of a magnetically shielded hall thruster *J. Propuls. Power* 1–18
- [23] Mikellides I G and Katz I 2012 Numerical simulations of Hall-effect plasma accelerators on a magnetic-field-aligned mesh *Phys. Rev. E* **86** 046703
- [24] Jorns B A, Goebel D M and Hofer R R 2015 Plasma perturbations in high-speed probing of Hall thruster discharge chambers: quantification and mitigation *51st Joint Propulsion Conf.* (AIAA American Institute of Aeronautics and Astronautics Inc) (<https://doi.org/10.2514/6.2015-4006>)
- [25] Hofer R R 2004 Development and characterization of high-efficiency, high-specific impulse xenon Hall thrusters *PhD Thesis* University of Michigan
- [26] Hofer R R and Gallimore A D 2006 High-specific impulse Hall thrusters, part 2: efficiency analysis *J. Propul. Power* **22** 732–40
- [27] Hofer R, Katz I, Goebel D, Jameson K, Sullivan R, Johnson L and Mikellides I 2008 Efficacy of electron mobility models in hybrid-PIC Hall thruster simulations *44th Joint Propulsion Conf. and Exhibit*, (Hartford, CT) (American Institute of Aeronautics and Astronautics) (<https://doi.org/10.2514/6.2008-4924>)
- [28] Goebel D M and Katz I 2008 *Fundamentals of Electric Propulsion: Ion and Hall Thrusters* (Jet Propulsion Laboratory, California Institute of Technology)
- [29] Mazouffre S, Bourgeois G, Garrigues L and Pawelec E 2011 A comprehensive study on the atom flow in the cross-field discharge of a Hall thruster *J. Phys. D: Appl. Phys.* **44** 105203
- [30] Dragnea H C, Lopez Ortega A, Kamhawi H and Boyd I D 2020 Simulation of a Hall effect thruster using krypton propellant *J. Propuls. Power* **36** 335–45
- [31] Rejoub R, Lindsay B G and Stebbings R F 2002 Determination of the absolute partial and total cross sections for electron-impact ionization of the rare gases *Phys. Rev. A* **65** 042713
- [32] Wetzel R C, Baiocchi F A, Hayes T R and Freund R S 1987 Absolute cross sections for electron-impact ionization of the rare-gas atoms by the fast-neutral-beam method *Phys. Rev. A* **35** 559
- [33] Katz I and Mikellides I G 2011 Neutral gas free molecular flow algorithm including ionization and walls for

- use in plasma simulations *J. Comput. Phys.* **230** 1454–64
- [34] Pan R, Ren J, Mao R and Tang H 2023 Practical analysis of different neutral algorithms for particle simulation of Hall thruster *Plasma Sources Sci. Technol.* **32** 034005
- [35] Mikellides I G and Lopez Ortega A 2019 Challenges in the development and verification of first-principles models in Hall-effect thruster simulations that are based on anomalous resistivity and generalized Ohm's law *Plasma Sources Sci. Technol.* **28** 014003
- [36] Hofer R R, Cusson S E, Lobbia R B and Gallimore A D 2017 The H9 magnetically shielded Hall thruster *35th Int. Electric Propulsion Conf. (Atlanta, GA)*
- [37] Su L L and Jorns B A 2021 Performance at high current densities of a magnetically-shielded Hall thruster *Propulsion and Energy Forum* (American Institute of Aeronautics and Astronautics) (<https://doi.org/10.2514/6.2021-3405>)
- [38] Su L L 2023 Performance of a magnetically shielded Hall thruster operating on krypton at high powers *PhD Thesis* University of Michigan (<https://doi.org/10.2027.42/192399>)
- [39] Viges E A, Jorns B A, Gallimore A D and Sheehan J P 2019 University of Michigan's upgraded large vacuum test facility *36th Int. Electric Propulsion Conf. (Vienna, Austria)*
- [40] Dankanich J W, Walker M, Swiatek M W and Yim J T 2017 Recommended practice for pressure measurement and calculation of effective pumping speed in electric propulsion testing *J. Propuls. Power* **33** 668–80
- [41] Peterson P Y, Kamhawi H, Huang W, Yim J, Herman D, Williams G, Gilland J and Hofer R 2016 NASA HERMeS Hall thruster electrical configuration characterization *52nd Joint Propulsion Conf.* (<https://doi.org/10.2514/6.2016-5027>)
- [42] Lopez Ortega A, Jorns B, Mikellides I G and Hofer R R 2015 Numerical simulations of the xr-5 Hall thruster for life assessment at different operating conditions *51st AIAA/SAE/ASEE Joint Propulsion Conf.* p 4008
- [43] Pierre Boeuf J 2017 Tutorial: physics and modeling of Hall thrusters *J. Appl. Phys.* **121** 011101
- [44] Marks T A and Jorns B A 2023 Challenges with the self-consistent implementation of closure models for anomalous electron transport in fluid simulations of Hall thrusters *Plasma Sources Sci. Technol.* **32** 045016
- [45] Georgin M P, Jorns B A and Gallimore A D 2020 Transient non-classical transport in the hollow cathode plume I: measurements of time-varying electron collision frequency *Plasma Sources Sci. Technol.* **29** 105010
- [46] Marks T A, Lopez Ortega A, Mikellides I G and Jorns B 2021 Self-consistent implementation of a zero-equation transport model into a predictive model for a Hall effect thruster *AIAA Propulsion and Energy 2021 Forum* p 3424
- [47] Cedolin R J, Hargus W A Jr, Storm P V, Hanson R K and Cappelli M A 1997 Laser-induced fluorescence study of a xenon Hall thruster *Appl. Phys. B* **65** 459–69
- [48] Hargus W A and Cappelli M A 2001 Laser-induced fluorescence measurements of velocity within a Hall discharge *Appl. Phys. B* **72** 961–9
- [49] Durot C J, Gallimore A D and Smith T B 2014 Validation and evaluation of a novel time-resolved laser-induced fluorescence technique *Rev. Sci. Instrum.* **85** 013508
- [50] Chaplin V H, Jorns B A, Lopez Ortega A, Mikellides I G, Conversano R W, Lobbia R B and Hofer R R 2018 Laser-induced fluorescence measurements of acceleration zone scaling in the 12.5 kW HERMeS Hall thruster *J. Appl. Phys.* **124** 183302
- [51] Dale E T 2020 Investigation of the Hall thruster breathing mode *PhD Thesis* University of Michigan
- [52] Kramida A,Ralchenko Y and Reader J (NIST ASD Team) 2021 NIST atomic spectra database (ver. 5.9) (available: <https://physics.nist.gov/asd>) (Accessed 5 April 2022) National Institute of Standards and Technology
- [53] Hargus W A, Azarnia G M and Nakles M R 2011 Demonstration of laser-induced fluorescence on a krypton Hall effect thruster *32nd Int. Electric Propulsion Conf.* (Wiesbaden, Germany)
- [54] Su L L, Marks T A and Jorns B A 2022 Investigation into the efficiency gap between krypton and xenon operation on a magnetically shielded Hall thruster *Int. Electric Propulsion Conf. (Boston, MA)* (Electric Rocket Propulsion Society)
- [55] Huang W, Drenkow B and Gallimore A 2009 Laser-induced fluorescence of singly-charged xenon inside a 6-kw Hall thruster *45th Joint Propulsion Conf. & Exhibit* p 5355
- [56] Efron B and Tibshirani R J 1994 *An Introduction to the Bootstrap* (CRC Press) (<https://doi.org/10.1201/9780429246593>)
- [57] Jorns B A, Dodson C A, Anderson J R, Goebel D M, Hofer R R, Sekerak M J, Lopez Ortega A and Mikellides I G 2016 Mechanisms for pole piece erosion in a 6-kw magnetically-shielded Hall thruster *52nd Joint Propulsion Conf.* p 4839
- [58] Huang W, Gallimore A D and Hofer R R 2011 Neutral flow evolution in a six-kilowatt Hall thruster *J. Propuls. Power* **27** 553–63
- [59] Mazouffre S 2012 Laser-induced fluorescence diagnostics of the cross-field discharge of Hall thrusters *Plasma Sources Sci. Technol.* **22** 013001
- [60] Gawron D, Mazouffre S, Sadeghi N and Héron A 2008 Influence of magnetic field and discharge voltage on the acceleration layer features in a Hall effect thruster *Plasma Sources Sci. Technol.* **17** 0–10
- [61] Cusson S E, Dale E T, Jorns B A and Gallimore A D 2019 Acceleration region dynamics in a magnetically shielded Hall thruster *Phys. Plasmas* **26** 023506
- [62] Hofer R, Goebel D, Mikellides I and Katz I 2012 Design of a laboratory Hall thruster with magnetically shielded channel walls, phase II: experiments *48th Joint Propulsion Conf. and Exhibit*, (Atlanta, GA) (American Institute of Aeronautics and Astronautics) (<https://doi.org/10.2514/6.2012-3788>)
- [63] Zharinov A V 1967 Acceleration of plasma by a closed hall current *Sov. Phys. Tech. Phys.* **12** 208–11
- [64] Raitses Y, Staack D, Smirnov A and Fisch N J 2005 Space charge saturated sheath regime and electron temperature saturation in Hall thrusters *Phys. Plasmas* **12** 073507
- [65] Staack D, Raitses Y and Fisch N J 2004 Temperature gradient in Hall thrusters *Appl. Phys. Lett.* **84** 3028–30
- [66] Reid B and Gallimore A 2008 Plasma potential measurements in the discharge channel of a 6-kw Hall thruster *Joint Propulsion Conf. and Exhibit* (AIAA) p 5185
- [67] Linnell J A and Gallimore A D 2006 Internal plasma potential measurements of a Hall thruster using xenon and krypton propellant *Phys. Plasmas* **13** 093502
- [68] Dale E T and Jorns B A 2021 Experimental characterization of Hall thruster breathing mode dynamics *J. Appl. Phys.* **130** 133302
- [69] Zhang G, Ren J, Tang H, Wang Y, Zhang Z, Liu J, Pan R, Zhang Z and Cao J 2023 Plasma diagnosis inside the discharge channel of a low-power Hall thruster working on xe/kr mixtures *Acta Astronaut.* **204** 389–401
- [70] Andreussi T, Saravia M M and Andrenucci M 2019 Plasma characterization in Hall thrusters by Langmuir probes *J. Instrum.* **14** C05011